

Optimizing MR Scan Design for Model-Based T_1 , T_2 Estimation From Steady-State Sequences

Gopal Nataraj*, Senior Member, IEEE, Jon-Fredrik Nielsen, and Jeffrey A. Fessler, Fellow, IEEE,

Abstract—Rapid, reliable quantification of MR relaxation parameters T_1 and T_2 is desirable for many clinical applications. Steady-state sequences such as Spoiled Gradient-Recalled Echo (SPGR) and Dual-Echo Steady-State (DESS) are fast and well-suited for relaxometry because the signals they produce are quite sensitive to T_1 and T_2 variation. However, T_1 , T_2 estimation with these sequences typically requires multiple scans with varied sets of acquisition parameters. This paper describes a systematic framework for selecting scan types (e.g., combinations of SPGR and DESS scans) and optimizing their respective parameters (e.g., flip angles and repetition times). The method is based on a Cramér-Rao Bound (CRB)-inspired min-max optimization that finds scan parameter combinations that robustly enable precise object parameter estimation. We apply this technique to optimize combinations of SPGR and DESS scans for T_1 , T_2 relaxometry in white matter (WM) and grey matter (GM) regions of the human brain at 3T field strength. Phantom accuracy experiments show that SPGR/DESS scan combinations are in excellent agreement with reference measurements. Phantom precision experiments show that trends in T_1 , T_2 pooled sample standard deviations reflect CRB-based predictions. *In vivo* experiments show that in WM and GM, T_1 and T_2 estimates from a pair of optimized DESS scans exhibit precision (but not necessarily accuracy) comparable to that of optimized combinations of SPGR and DESS scans. To our knowledge, T_1 maps from DESS acquisitions alone are new. This example application illustrates that scan optimization may help reveal new parameter mapping techniques from combinations of established pulse sequences.

Index Terms— T_1 , T_2 relaxometry, optimal experimental design, Cramér-Rao bound, magnetic resonance imaging.

I. INTRODUCTION

FAST, accurate quantification of spin-lattice and spin-spin relaxation parameters T_1 and T_2 has been of longstanding interest in MRI. Many researchers have suggested that T_1 , T_2

Manuscript received August 11, 2016; revised September 27, 2016; accepted September 29, 2016. Date of publication October 4, 2016; date of current version February 1, 2017. This work was supported in part by the National Institutes of Health (NIH) under Grant P01 CA87634 and in part by the University of Michigan MCubed seed grant program. *Asterisk indicates corresponding author.*

*G. Nataraj is with the Department of Electrical Engineering and Computer Science, University of Michigan, Ann Arbor, MI 48109 USA (e-mail: gnataraj@umich.edu).

J.-F. Nielsen is with the Department of Biomedical Engineering, University of Michigan, Ann Arbor, MI 48109 USA (e-mail: jfnielse@umich.edu).

J. A. Fessler is with the Department of Electrical Engineering and Computer Science, University of Michigan, Ann Arbor, MI 48109 USA (e-mail: fessler@umich.edu).

This paper has supplementary downloadable material available at <http://ieeexplore.ieee.org>, provided by the author.

Digital Object Identifier 10.1109/TMI.2016.2614967

maps may serve as biomarkers for monitoring the progression of various disorders [1]. Neurological applications include: lesion classification in multiple sclerosis [2]; tumor characterization [3], [4]; and symptom onset prediction in stroke [5], [6]. In addition, T_1 , T_2 have shown promise for detecting hip and knee cartilage degeneration [7], [8] and for assessing cardiac dysfunction due to iron overload [9] or edema [10]. Motivated by this broad interest in T_1 , T_2 mapping, this paper describes a systematic method to guide MR scan design.

Classical pulse sequences such as inversion/saturation recovery (IR/SR) or (single) spin echo (SE) yield relatively simple methods for T_1 or T_2 estimation, respectively; however, these methods require several scans, each with long repetition time T_R , leading to undesirably long acquisitions. Numerous modifications such as the Look-Locker method [11], multi-SE trains [12], or fast k -space trajectories [13]–[15] have been proposed to accelerate T_1 [16]–[19] and T_2 [20]–[23] relaxometry with these classical sequences. These techniques are more sensitive to model non-idealities [24]–[26], and are still speed-limited by the long T_R required for (near)-complete T_1 recovery.

Steady-state (SS) pulse sequences [27], [28] permit short T_R , and are thus inherently much faster than classical counterparts. SS techniques are well-suited for relaxometry because the signals produced are highly sensitive to T_1 and T_2 variation. However, short T_R times also cause SS signals to be complex functions of both desired and undesired (*nuisance*) parameters, complicating quantification. Furthermore, some such methods [29], [30] still require scan repetition, though individual scans are now considerably shorter. Despite these difficulties, the potential for rapid scanning with high T_1 , T_2 sensitivity has motivated numerous SS relaxometry studies [29]–[38].

The dual-echo steady-state (DESS) sequence [39] was recently proposed as a promising SS imaging technique for T_2 estimation [35]. Because it produces two distinct signals per excitation, the DESS sequence can reduce scan repetition requirements by recording twice as much data per scan. As with other SS methods, the resulting signals [40], [41] are complicated functions of T_1 , T_2 , and other parameters. Prior works have isolated T_2 dependencies using either algebraic manipulations of the first- and second-echo signals [35], [36] or separate scans to first estimate nuisance parameters [42]. Although DESS concurrently encodes rich T_1 and T_2 information, these methods have shied away from using DESS for T_1 estimation, either through bias-inducing approximations, or noise-propagating sequential estimation, respectively.

Whether it be with DESS, other sequences, or even combinations thereof, it is generally unclear how to best assemble a *scan profile* (i.e., a collection of scans) for a fixed amount of scan time. Furthermore, for a given scan profile, it is typically not obvious how to best select acquisition parameters (e.g., flip angles, repetition times, etc.) for relaxometry. In this paper, the term *scan design* refers to the related problems of scan profile selection and scan parameter optimization.

Historically, scan design for relaxometry has predominantly been explored using figures of merit related to estimator precision. In particular, several studies have used the Cramér-Rao Bound (CRB), a statistical measure that bounds the minimum variance of an unbiased estimator. Earlier works have used the CRB and variations to select inversion times for recovery experiments [43], [44], flip angles for spoiled gradient-recalled echo (SPGR) sequences [45], and echo times for SE experiments [46]. More recent studies have considered additional scan design challenges, including scan time constraints [47], multiple latent parameters [48], multiple scan parameter types [49], and latent parameter spatial variation [50], [51].

The aforementioned studies consider scan parameter optimization for profiles consisting of *only one* pulse sequence. In contrast, this paper introduces a general framework for robust, application-specific scan design for parameter estimation from *combinations* of pulse sequences. The framework first finds multiple sets of scan parameters that achieve precise estimation within a tight, *application-specific* range of object parameters (e.g., T_1 , T_2 , etc.). The framework then chooses the one scan parameter set most *robust* to estimator precision degradation over a broader range of object parameters. As a detailed example, we optimize three combinations of DESS and SPGR sequences for T_1 , T_2 mapping. For a fixed total scan time, we find that well-chosen DESS scans alone can be used to estimate both T_1 and T_2 with precision and robustness comparable to combinations of DESS and SPGR. This example illustrates that, with careful scan profile design, well-established pulse sequences can find use in new estimation problems.

This paper is organized as follows. Section II uses a general signal model to describe a CRB-inspired min-max optimization problem for robust, application-specific scan optimization. Section III adapts the DESS signal models to our framework and optimizes three practical DESS/SPGR combinations to show that, even in the presence of radiofrequency (RF) field inhomogeneity, DESS is a promising option for T_1 , T_2 relaxometry. Section IV describes simulation, phantom, and *in vivo* experiments and discusses corresponding results. Section V discusses practical challenges and suggests future directions. Section VI summarizes key contributions.

II. A CRB-INSPIRED SCAN SELECTION METHOD

A. A Generalized Signal Model

A broad class of MR pulse sequences useful for parameter mapping produce, after reconstruction, a set of noisy images $y_d(\cdot)$ that can be described with the following general model:

$$y_d(\mathbf{r}) = f_d(\mathbf{x}(\mathbf{r}); \mathbf{v}(\mathbf{r}), \mathbf{p}_d) + \epsilon_d(\mathbf{r}), \quad d = 1, \dots, D, \quad (1)$$

where $\mathbf{x}(\mathbf{r}) \in \mathbb{C}^L$ collects L *latent* object parameters, at position \mathbf{r} ; $\mathbf{v}(\mathbf{r}) \in \mathbb{C}^K$ gathers K *known* object parameters at \mathbf{r} ; $\mathbf{p}_d \in \mathbb{R}^P$ denotes a set of P scan parameters chosen for the d th dataset; $f_d : \mathbb{C}^L \times \mathbb{C}^K \times \mathbb{R}^P \mapsto \mathbb{C}$ is a (pulse-sequence dependent) function that models the noiseless signal obtained from the d th dataset; and $\epsilon_d \sim \mathcal{CN}(0, \sigma_d^2)$ is assumed, for sake of simplicity, to be independent, complex Gaussian noise¹ [54], [55]. (As a concrete example, for $T_2(\cdot)$ mapping from single SE datasets, $\mathbf{x}(\cdot)$ could collect spin density and $T_2(\cdot)$; $\mathbf{v}(\cdot)$ could collect known off-resonance and RF field inhomogeneities; and \mathbf{p}_d could assign the d th echo time, chosen to yield image $y_d(\cdot)$.)

A scan profile consists of D datasets from a combination of pulse sequences. Let $\mathbf{y}(\mathbf{r}) := [y_1(\mathbf{r}), \dots, y_D(\mathbf{r})]^\top \in \mathbb{C}^D$ collect the noisy signals at \mathbf{r} from all datasets, $\mathbf{P} := [\mathbf{p}_1, \dots, \mathbf{p}_D] \in \mathbb{R}^{P \times D}$ gather the corresponding scan parameters, and vector function $\mathbf{f} : \mathbb{C}^L \times \mathbb{C}^K \times \mathbb{R}^{P \times D} \mapsto \mathbb{C}^D$ naturally extend scalar function f , where $(\cdot)^\top$ denotes vector transpose. Then the log-likelihood function is (to within a constant independent of $\mathbf{x}(\mathbf{r})$):

$$\ln L(\mathbf{x}(\mathbf{r})) = -\frac{1}{2} \|\mathbf{y}(\mathbf{r}) - \mathbf{f}(\mathbf{x}(\mathbf{r}); \mathbf{v}(\mathbf{r}), \mathbf{P})\|_{\Sigma}^2, \quad (2)$$

where covariance matrix $\Sigma := \text{diag}(\sigma_1^2, \dots, \sigma_D^2)$ is diagonal due to the assumption of independence between scans.

Under suitable regularity conditions², the Fisher information matrix $\mathbf{I}(\mathbf{x}(\mathbf{r}); \mathbf{v}(\mathbf{r}), \mathbf{P}) \in \mathbb{C}^{L \times L}$ [56] is a measure useful for characterizing the precision of unbiased estimates of $\mathbf{x}(\mathbf{r})$ from $\mathbf{y}(\mathbf{r})$, given $\mathbf{v}(\mathbf{r})$ and \mathbf{P} :

$$\begin{aligned} \mathbf{I}(\mathbf{x}(\mathbf{r}); \mathbf{v}(\mathbf{r}), \mathbf{P}) &:= \mathbb{E} \left([\nabla_{\mathbf{x}} \ln L(\mathbf{x}(\mathbf{r}))]^\dagger [\nabla_{\mathbf{x}} \ln L(\mathbf{x}(\mathbf{r}))] \right) \\ &= [\nabla_{\mathbf{x}} \mathbf{f}(\mathbf{x}(\mathbf{r}); \mathbf{v}(\mathbf{r}), \mathbf{P})]^\dagger \\ &\quad \times \Sigma^{-1} [\nabla_{\mathbf{x}} \mathbf{f}(\mathbf{x}(\mathbf{r}); \mathbf{v}(\mathbf{r}), \mathbf{P})], \end{aligned} \quad (3)$$

where $\mathbb{E}(\cdot)$ denotes expectation; $\nabla_{\mathbf{x}}$ denotes a row gradient with respect to \mathbf{x} at fixed \mathbf{r} ; and $(\cdot)^\dagger$ denotes Hermitian transpose. In particular, the matrix Cramér-Rao Bound (CRB) [57] ensures that any unbiased estimator $\hat{\mathbf{x}}(\mathbf{r})$ satisfies

$$\text{cov}(\hat{\mathbf{x}}(\mathbf{r}); \mathbf{v}(\mathbf{r}), \mathbf{P}) \succeq \mathbf{I}^{-1}(\mathbf{x}(\mathbf{r}); \mathbf{v}(\mathbf{r}), \mathbf{P}), \quad (4)$$

where for arbitrary, equally sized matrices \mathbf{A} and \mathbf{B} , matrix inequality $\mathbf{A} \succeq \mathbf{B}$ means $\mathbf{A} - \mathbf{B}$ is positive semi-definite. In the following, we design an optimization problem based on the CRB to guide MR scan design for relaxometry.

B. Min-Max Optimization Problem for Scan Design

Following [58], we focus on minimizing a weighted average of the variances in each of the L latent object parameter estimates. A reasonable objective function for overall estimator

¹Though the noise distribution of \mathbf{k} -space raw data is usually well-modeled as complex white Gaussian, the noise distribution of the d th reconstructed image $y_d(\cdot)$ depends both on the acquisition and reconstruction. If single receive channel \mathbf{k} -space data is fully-sampled on a Cartesian grid, each dataset $y_d(\cdot)$ is recoverable via separate Fourier transform, and is thus complex Gaussian and independent across datasets. However, if \mathbf{k} -space data is multi-channel, undersampled, and/or non-Cartesian, it may be preferable that $y_d(\cdot)$ be estimated by more sophisticated techniques, e.g., [52], [53]. In such cases, reconstructed image noise is unlikely to be Gaussian-distributed.

²In particular, \mathbf{f} must be analytic in complex components of \mathbf{x} at each \mathbf{r} .

precision is therefore given by

$$\Psi(\mathbf{x}(\mathbf{r}); \mathbf{v}(\mathbf{r}), \mathbf{P}) = \text{tr} \left(\mathbf{W} \mathbf{I}^{-1}(\mathbf{x}(\mathbf{r}); \mathbf{v}(\mathbf{r}), \mathbf{P}) \mathbf{W}^T \right), \quad (5)$$

where $\mathbf{W} \in \mathbb{R}^{L \times L}$ is a diagonal, application-specific matrix of weights, preselected to control the relative importance of precisely estimating the L latent object parameters; and $\text{tr}(\cdot)$ denotes the matrix trace operation. For scan design, we would like to minimize (5) with respect to scan parameters \mathbf{P} .

The CRB depends not only on \mathbf{P} but also on the spatially varying object parameters $\mathbf{x}(\cdot)$ and $\mathbf{v}(\cdot)$. Thus, one cannot perform scan design by “simply” minimizing Ψ over the scan parameters \mathbf{P} . Instead, we pose a practical and application-dependent *min-max* optimization problem for scan design: we seek candidate scan parameters \mathbf{P} over a search space \mathcal{P} that *minimize* the worst-case, *i.e.*, *maximum* cost $\tilde{\Psi}^t$, as viewed over “tight” parameter ranges \mathcal{X}_t and \mathcal{N}_t :

$$\check{\mathbf{P}} \in \arg \min_{\mathbf{P} \in \mathcal{P}} \tilde{\Psi}^t(\mathbf{P}), \quad \text{where} \quad (6)$$

$$\tilde{\Psi}^t(\mathbf{P}) = \max_{\substack{\mathbf{x} \in \mathcal{X}_t \\ \mathbf{v} \in \mathcal{N}_t}} \Psi(\mathbf{x}; \mathbf{v}, \mathbf{P}). \quad (7)$$

Here, we select *latent* object parameter set \mathcal{X}_t based on the application and *known* parameter set \mathcal{N}_t based on the spatial variation typically observed in the known parameters $\mathbf{v}(\cdot)$. Min-max approach (6) should ensure good estimation precision over a range of parameter values.

Since Ψ is in general non-convex with respect to \mathbf{P} , it may have multiple global minimizers as well as other scan parameters that are nearly global minimizers. To improve robustness to object parameter variations, we form an expanded set of candidate parameter values by also including scan parameters that yield costs to within a tolerance $\delta \ll 1$ of the optimum. Mathematically, we define this expanded set of candidate scan parameter combinations (for a given scan profile) as

$$\mathcal{S} := \left\{ \mathbf{P} : \tilde{\Psi}^t(\mathbf{P}) - \tilde{\Psi}^t(\check{\mathbf{P}}) \leq \delta \tilde{\Psi}^t(\check{\mathbf{P}}) \right\}. \quad (8)$$

To select amongst these candidate scan parameters, we employ a robustness criterion: we select the single scan parameter \mathbf{P}^* that degrades the least when the worst-case cost is viewed over widened object parameter sets $\mathcal{X}_b \supseteq \mathcal{X}_t$ and $\mathcal{N}_b \supseteq \mathcal{N}_t$:

$$\mathbf{P}^* = \arg \min_{\mathbf{P} \in \mathcal{S}} \tilde{\Psi}^b(\mathbf{P}), \quad \text{where} \quad (9)$$

$$\tilde{\Psi}^b(\mathbf{P}) = \max_{\substack{\mathbf{x} \in \mathcal{X}_b \\ \mathbf{v} \in \mathcal{N}_b}} \Psi(\mathbf{x}; \mathbf{v}, \mathbf{P}). \quad (10)$$

To compare different scan profiles, we select corresponding search spaces \mathcal{P} to satisfy acquisition constraints (*e.g.*, total scan time), but otherwise hold optimization parameters \mathbf{W} , δ , $\mathcal{X}_{t,b}$, and $\mathcal{N}_{t,b}$ fixed. Since Ψ is data-independent, we can solve (6) and (9) offline for each scan profile. The result of each profile’s min-max optimization process (9) is a corresponding optimized scan parameter matrix \mathbf{P}^* that is suitable for the range of latent \mathbf{x} and known \mathbf{v} object parameters specified in \mathcal{X}_t and \mathcal{N}_t , and is robust to variations in those parameters over broader sets \mathcal{X}_b and \mathcal{N}_b , respectively.

III. APPLICATION: OPTIMIZING SS SEQUENCES FOR T_1 , T_2 RELAXOMETRY IN THE BRAIN

This section applies the methods of Section II-B to the problem of scan design for joint T_1, T_2 estimation from combinations of SS sequences. Section III-A presents a brief overview of the DESS signals, formulating models to permit estimation of as few nuisance parameters as possible. Section III-B details how we use optimization problems (6) and (9) to tailor three combinations of DESS and SPGR scans for precise T_1, T_2 estimation in white matter (WM) and grey matter (GM) regions of the human brain. Section III-C compares the predicted performance of the three optimized scan profiles.

A. The DESS Signal Model

The DESS sequence interlaces RF excitations with unbalanced spoiler gradients of fixed area [39] to produce two distinct signals per excitation. If the gradient lobe area is carefully chosen to dominate through-voxel field inhomogeneity gradients, yet not introduce significant diffusive effects [59]–[61], the bulk steady-state signal s_D (from a voxel centered at position \mathbf{r}) immediately *before* ($t \approx 0^-$) and *after* ($t \approx 0^+$) an RF excitation centered at time $t = 0$ can be written as

$$s_D(\mathbf{r}, 0^-) = -i M_0(\mathbf{r}) \tan \frac{\alpha(\mathbf{r})}{2} [1 - \eta(\mathbf{r}, T_R)] \quad \text{and} \quad (11)$$

$$s_D(\mathbf{r}, 0^+) = i M_0(\mathbf{r}) \tan \frac{\alpha(\mathbf{r})}{2} \left[1 - \frac{\eta(\mathbf{r}, T_R)}{\zeta(\mathbf{r}, T_R)} \right]; \quad \text{where} \quad (12)$$

$$\eta(\mathbf{r}, t) := \sqrt{\frac{1 - E_2^2(\mathbf{r}, t)}{1 - E_2^2(\mathbf{r}, t)/\xi^2(\mathbf{r}, t)}}, \quad \text{and} \quad (13)$$

$$\zeta(\mathbf{r}, t) := \frac{1 - E_1(\mathbf{r}, t) \cos \alpha(\mathbf{r})}{E_1(\mathbf{r}, t) - \cos \alpha(\mathbf{r})}. \quad (14)$$

Here, $E_u(\mathbf{r}, t) := \exp(-t/T_u(\mathbf{r}))$ for $u \in \{1, 2\}$ describes longitudinal or transverse relaxation at time t , respectively; $M_0(\mathbf{r}) \in \mathbb{C}$ is proportional to spin density; flip angle $\alpha(\mathbf{r}) = \alpha_0 \kappa(\mathbf{r})$ is decomposed as a nominal (prescribed) value α_0 with spatial variation $\kappa(\mathbf{r}) \approx 1$ due to RF field inhomogeneities; T_R is repetition time; and $i := \sqrt{-1}$. Signal models (11) and (12) neglect relaxation and off-resonance effects during each (short) RF pulse³, and assume RF rotations about the \hat{i} -axis.

We model each voxel’s macroscopic broadening distribution to be Cauchy($\bar{\omega}(\mathbf{r}), R'_2(\mathbf{r})$), where $\bar{\omega}(\mathbf{r})$ denotes median off-resonance frequency and $R'_2(\mathbf{r})$ is the broadening bandwidth. If we time readout gradients to form echoes symmetrically centered at echo time T_E before and after RF excitation, then the noiseless DESS signals are well approximated as

$$s_D(\mathbf{r}, -T_E) \approx s_D(\mathbf{r}, 0^-) E_2^{-1}(\mathbf{r}, T_E) e^{-(R'_2(\mathbf{r}) + i\bar{\omega}(\mathbf{r}))T_E} \quad (15)$$

$$s_D(\mathbf{r}, +T_E) \approx s_D(\mathbf{r}, 0^+) E_2(\mathbf{r}, T_E) e^{-(R'_2(\mathbf{r}) - i\bar{\omega}(\mathbf{r}))T_E}. \quad (16)$$

³Finite-duration RF effects influence SS signals more strongly for shorter T_R , larger α_0 , and smaller T_2/T_1 [62]. In this work, RF pulse durations do not exceed 11% of repetition times and do not excite nominal flip angles greater than 35°. Phantom results (*cf.* Fig. 1) show that for these scan parameters, the influence of finite-duration RF effects on T_1, T_2 estimates is small even for $T_2/T_1 \approx 0.1$ as in WM/GM.

In (15) and (16), nuisance parameters $M_0(\mathbf{r})$, $R'_2(\mathbf{r})$, $\kappa(\mathbf{r})$, and $\tilde{\omega}(\mathbf{r})$ complicate estimation of $T_1(\mathbf{r})$ and $T_2(\mathbf{r})$. For simplicity, we take $\kappa(\mathbf{r})$ to be known from a separately acquired RF transmit field $B_1^+(\mathbf{r})$ scan. To avoid (separate or joint) $\tilde{\omega}(\mathbf{r})$ estimation, we choose to use magnitude DESS data, at the expense of slight model mismatch (studied with simulations in Section IV-A) in (1) due to Rician noise. By fixing T_E across acquisitions and defining

$$M_E(\mathbf{r}) := M_0(\mathbf{r})E_2(\mathbf{r}, T_E)e^{-R'_2(\mathbf{r})T_E}, \quad (17)$$

we can rewrite magnitude signals as functions of $L = 3$ latent and $K = 1$ known object parameters, collected as $\mathbf{x}(\mathbf{r}) := [M_E(\mathbf{r}), T_1(\mathbf{r}), T_2(\mathbf{r})]^T$ and $\nu(\mathbf{r}) := \kappa(\mathbf{r})$, respectively:

$$\begin{aligned} f_1(\mathbf{x}(\mathbf{r}); \nu(\mathbf{r}), \mathbf{p}) &:= |s_D(\mathbf{r}, -T_E)| \\ &= M_E(\mathbf{r}) \tan \frac{\alpha(\mathbf{r})}{2} E_2^{-2}(\mathbf{r}, T_E) [1 - \eta(\mathbf{r}, T_R)] \end{aligned} \quad (18)$$

$$\begin{aligned} f_2(\mathbf{x}(\mathbf{r}); \nu(\mathbf{r}), \mathbf{p}) &:= |s_D(\mathbf{r}, +T_E)| \\ &= M_E(\mathbf{r}) \tan \frac{\alpha(\mathbf{r})}{2} \left[1 - \frac{\eta(\mathbf{r}, T_R)}{\xi(\mathbf{r}, T_R)} \right]; \end{aligned} \quad (19)$$

where $\mathbf{p} := [\alpha_0, T_R]^T$ collects the $P = 2$ scan parameters we are free to optimize. From here, we use the scan design method described in Section II to select an optimized \mathbf{p} corresponding to each DESS scan within a particular scan profile.

B. Scan Design Details

There are numerous candidate scan profiles involving DESS and/or other pulse sequences that may be useful for fast, accurate T_1, T_2 mapping. In this work, we consider combinations of DESS and SPGR scans [63]. With proper RF phase cycling and gradient spoiling, the SPGR signal s_S can be expressed without any explicit $T_2(\mathbf{r})$ dependence:

$$s_S(\mathbf{r}, T_E) = \frac{i M_E(\mathbf{r}) \sin \alpha(\mathbf{r}) (1 - E_1(\mathbf{r}, T_R))}{1 - E_1(\mathbf{r}, T_R) \cos \alpha(\mathbf{r})}. \quad (20)$$

SPGR's reduced dependence on spatially varying unknowns is reason for its use for T_1 mapping [30]–[32] and subsequent T_2 mapping from other sequences [29], [42]. In a similar spirit, we examine scan profiles containing SPGR over other SS sequences because we predict that the SPGR sequence's T_2 -independence may help estimators disentangle T_2 from other unknown sources of DESS signal contrast.

As written in (20), each SPGR scan also leaves $\mathbf{p} = [\alpha_0, T_R]^T$ as $P = 2$ scan parameters available to optimize. A given scan profile consisting of C_{SPGR} SPGR and C_{DESS} DESS scans yields $D = C_{\text{SPGR}} + 2C_{\text{DESS}}$ datasets. We optimize such a scan profile by solving (9) over a dimension- $PD = 2(C_{\text{SPGR}} + 2C_{\text{DESS}})$ space of scan parameters.

We select constraints on search space \mathcal{P} based on hardware limitations and desired scan profile properties. Since each pair of DESS signals must share the same choice of \mathbf{p} , the search space is reduced to $\mathcal{A}_{0,\text{SPGR}}^{C_{\text{SPGR}}} \times \mathcal{A}_{0,\text{DESS}}^{C_{\text{DESS}}} \times \mathcal{T}_{R,\text{SPGR}}^{C_{\text{SPGR}}} \times \mathcal{T}_{R,\text{DESS}}^{C_{\text{DESS}}}$ (superscripts denote Cartesian powers). We assign flip angle ranges $\mathcal{A}_{0,\text{SPGR}} = \mathcal{A}_{0,\text{DESS}} \leftarrow [5, 90]^\circ$

to restrict RF energy deposition. We set feasible T_R solution sets $\mathcal{T}_{R,\text{SPGR}} \leftarrow [12.2, +\infty)$ ms and $\mathcal{T}_{R,\text{DESS}} \leftarrow [17.5, +\infty)$ ms based on pulse sequence designs that control for other scan parameters. These control parameters are described in further detail in Section IV, and are held fixed in all subsequent SPGR and DESS experiments. To equitably compare optima from different scan profiles, we require $\mathbf{T}_R := [T_{R,1}, \dots, T_{R,C_{\text{SPGR}}}, T_{R,C_{\text{SPGR}}+1}, \dots, T_{R,C_{\text{SPGR}}+C_{\text{DESS}}}]^T$ to satisfy a total time constraint, $\|\mathbf{T}_R\|_1 \leq T_{R,\text{max}}$. For a scan profile consisting of C_{SPGR} SPGR and C_{DESS} DESS scans, these constraints collectively reduce the search space dimension from PD to $2(C_{\text{SPGR}} + C_{\text{DESS}}) - 1$.

Prior works have considered T_1 or T_2 estimation from as few as 2 SPGR [29], [45] or 1 DESS [35] scan(s), respectively. We likewise elect to optimize the $(C_{\text{SPGR}}, C_{\text{DESS}}) \leftarrow (2, 1)$ scan profile as a benchmark. We choose $T_{R,\text{max}} \leftarrow 2(12.2) + 1(17.5) = 41.9$ ms and select other scan profiles capable of meeting this time constraint. Requiring that candidate profiles contain $C_{\text{DESS}} \geq 1$ DESS scans for T_2 contrast and satisfy $D \geq L (= 3)$ for well-conditioned estimation, we note that (1, 1) and (0, 2) are the only other eligible profiles.

In the ensuing experiments, we focus on precise T_1, T_2 estimation in the brain and design latent object parameter ranges $\mathcal{X}_t = \mathcal{M}_{E,t} \times \mathcal{T}_{1,t} \times \mathcal{T}_{2,t}$ and $\mathcal{N}_t = \mathcal{K}_t$ accordingly. Noting that $T_1 \sim 10T_2$, we choose $\mathbf{W} \leftarrow \text{diag}(0, 0.1, 1)$ in (5) to place roughly equal importance on precise T_1 vs. T_2 estimation. Since \mathbf{W} places zero weight on M_E estimation (obviating the need for complex differentiation in (3)), it is easily shown that Ψ depends on M_E only through a constant scale factor; thus it suffices to consider $\mathcal{M}_{E,t} \leftarrow 1$. We select $\mathcal{T}_{1,t} \leftarrow [800, 1400]$ ms and $\mathcal{T}_{2,t} \leftarrow [50, 120]$ ms to correspond with WM and GM regions of interest (ROIs) at 3T [64], [65]. We take $\mathcal{K}_t \leftarrow [0.9, 1.1]$ to account for 10% spatial variation in flip angle. Broadened ranges $\mathcal{X}_b \leftarrow 1 \times [400, 2000]$ ms \times [40, 200]ms and $\mathcal{K}_b \leftarrow [0.5, 2]$ are constructed to encourage solutions robust to a wide range of object parameters. We assume constant noise variance $\sigma_1^2 = \dots = \sigma_D^2 := \sigma^2$, where $\sigma^2 \leftarrow 1.49 \times 10^{-7}$ is selected to reflect measurements from normalized phantom datasets (*cf.* Sections IV.B.1 and S.V.A-S.V.B for acquisition details). Lastly, we set $\delta \leftarrow 0.01$ to select a robust scan parameter \mathbf{P}^* with associated worst-case cost $\tilde{\Psi}^t(\mathbf{P}^*)$ within 1% of global optimum $\tilde{\Psi}^t(\tilde{\mathbf{P}})$.

C. Scan Profile Comparisons

We solve (6) and (9) via grid search to allow illustration (§S.I in Supplement⁴) of $\tilde{\Psi}^t(\mathbf{P})$ as well as worst-case T_1, T_2 standard deviations $\tilde{\sigma}_{T_1}^t(\mathbf{P})$ and $\tilde{\sigma}_{T_2}^t(\mathbf{P})$, each defined as

$$\tilde{\sigma}_{T_1}^t(\mathbf{P}) := \max_{\substack{\mathbf{x} \in \mathcal{X}_b \\ \nu \in \mathcal{N}_b}} \sigma_{T_1}(\mathbf{x}; \nu, \mathbf{P}) \quad \text{and} \quad (21)$$

$$\tilde{\sigma}_{T_2}^t(\mathbf{P}) := \max_{\substack{\mathbf{x} \in \mathcal{X}_b \\ \nu \in \mathcal{N}_b}} \sigma_{T_2}(\mathbf{x}; \nu, \mathbf{P}), \quad (22)$$

where $\sigma_{T_1}(\mathbf{x}; \nu, \mathbf{P})$ and $\sigma_{T_2}(\mathbf{x}; \nu, \mathbf{P})$ are corresponding diagonal elements of inverse Fisher matrix $\mathbf{I}^{-1}(\mathbf{x}; \nu, \mathbf{P})$. Grid searches for the (2, 1), (1, 1), and (0, 2) profiles each took

⁴Supplementary material is available in the /media tab on IEEEXplore.

TABLE I

PERFORMANCE SUMMARY OF DIFFERENT SCAN PROFILES, OPTIMIZED BY SOLVING (9) SUBJECT TO SCAN TIME CONSTRAINT $T_{R,\max} = 41.9$ ms. THE FIRST COLUMN DEFINES EACH PROFILE. THE NEXT FOUR COLUMNS DESCRIBE \mathbf{P}^* . THE LATTER THREE PAIRS OF COLUMNS SHOW HOW WORST-CASE $\tilde{\sigma}_{T_1}^t$, $\tilde{\sigma}_{T_2}^t$, AND $\tilde{\Psi}$ VALUES DEGRADE FROM TIGHT TO BROAD RANGES. FLIP ANGLES ARE IN DEGREES; ALL OTHER VALUES ARE IN MILLISECONDS

Scan	$\hat{\alpha}_0^{\text{SPGR}}$	$\hat{\alpha}_0^{\text{DESS}}$	\hat{T}_R^{SPGR}	\hat{T}_R^{DESS}	$\tilde{\sigma}_{T_1}^t(\mathbf{P}^*)$	$\tilde{\sigma}_{T_1}^b(\mathbf{P}^*)$	$\tilde{\sigma}_{T_2}^t(\mathbf{P}^*)$	$\tilde{\sigma}_{T_2}^b(\mathbf{P}^*)$	$\tilde{\Psi}^t(\mathbf{P}^*)$	$\tilde{\Psi}^b(\mathbf{P}^*)$
(2, 1)	(15, 5) $^\circ$	30 $^\circ$	(12.2, 12.2)	17.5	28	154	1.3	9.1	4.0	17.7
(1, 1)	15 $^\circ$	10 $^\circ$	13.9	28.0	27	169	2.8	8.8	4.9	17.9
(0, 2)	–	(35, 10) $^\circ$	–	(24.4, 17.5)	21	113	1.5	6.0	3.5	12.2

about 4, 43, and 28 minutes, respectively. All experiments described hereafter were carried out using MATLAB® R2013a on a 3.5 GHz desktop with 32 GB RAM.

Table I compares optimized scan parameters for profiles consisting of (2, 1), (1, 1), and (0, 2) SPGR and DESS scans, respectively. In addition to $\tilde{\sigma}_{T_1}^t(\mathbf{P}^*)$ and $\tilde{\sigma}_{T_2}^t(\mathbf{P}^*)$, Table I presents analogous worst-case standard deviations $\tilde{\sigma}_{T_1}^b(\mathbf{P})$ and $\tilde{\sigma}_{T_2}^b(\mathbf{P})$ over $\mathcal{X}_b \times \mathcal{K}_b$ to show how each estimator degrades over the broadened object parameter range. When viewed over tight range $\mathcal{X}_t \times \mathcal{K}_t$, the (0, 2) profile provides a 11.5% reduction in worst-case cost over the other choices. Extending to broadened range $\mathcal{X}_b \times \mathcal{K}_b$, this reduction grows dramatically to 31.4%. We thus observe that while the different optimized profiles afford similar estimator precision over a narrow range of interest, the (0, 2) profile may be preferable due to its robustness to a wide range of object parameters.

As the DESS sequence has already found success for T_2 mapping from even one scan [35], it is reassuring but unsurprising that our analysis finds two DESS scans to yield the most precise T_2 estimates. More interestingly, our methods suggest that, with a minimum $C_{\text{DESS}} = 2$ scans, DESS can be used to simultaneously estimate T_1 as well. In fact, for certain choices of parameter ranges, a second DESS scan is predicted to afford \hat{T}_1 precision comparable to two SPGR scans.

IV. EXPERIMENTAL VALIDATION AND RESULTS

To test our approach to optimized scan design (described in Section II-B), we next estimate \mathbf{T}_1 and \mathbf{T}_2 maps (using maximum-likelihood (ML) and regularized least squares (RLS) methods detailed in Section S.II) from datasets collected using the scan profiles optimized in Section III. In Section IV-A, we study estimator statistics from simulated data. In Sections IV.B-IV.C, we progress to phantom and *in vivo* datasets to evaluate scan profile performance and estimator robustness under increasingly complex settings. For the latter experiments, we use reference parameter maps from classical (long) pulse sequences, in lieu of ground truth maps.

A. Numerical Simulations

We select T_1 and T_2 WM and GM values based on previously reported measurements at 3T [64], [65] and extrapolate other unimportant latent object parameters M_0 and T_2^* from measurements at 1.5T [66]. We assign these parameter values to the discrete anatomy of the BrainWeb digital phantom [66], [67] to create ground truth \mathbf{M}_0 , \mathbf{T}_1 , \mathbf{T}_2 , and \mathbf{T}_2^* maps.

We then choose acquisition parameters based on Table I (with fixed $T_E = 4.67$ ms) and apply models (20) and (15)–(16) to the 81st slices of these true maps to compute noiseless 217×181 SPGR and DESS image-domain data, respectively.

For each scan profile, we corrupt the corresponding (complex) noiseless dataset \mathbf{F} with additive complex Gaussian noise, whose variance $\sigma^2 \leftarrow 1.49 \times 10^{-7}$ is set to match CRB calculations. This yields realistically noisy datasets \mathbf{Y} ranging from 105-122 SNR, where SNR is defined here as

$$\text{SNR}(\mathbf{F}, \mathbf{Y}) := \frac{\|\mathbf{F}\|_F}{\|\mathbf{Y} - \mathbf{F}\|_F}. \quad (23)$$

We use each profile's noisy magnitude dataset $|\mathbf{Y}|$ to compute estimates $\hat{\mathbf{M}}_E$, $\hat{\mathbf{T}}_1$, and $\hat{\mathbf{T}}_2$ (images and histograms in Section S.III). We then evaluate estimator bias and variance from latent ground truth \mathbf{T}_1 and \mathbf{T}_2 maps.

In these simulations, we intentionally neglect to model a number of physically realistic effects because their inclusion would complicate study of estimator statistics. First and foremost, we assume knowledge of a uniform transmit field, to avoid confounding B_1^+ and T_1, T_2 estimation errors. For a similar reason, spatial variation in the sensitivity of a single receive coil is also not considered. We omit modeling partial volume effects to ensure deterministic knowledge of WM and GM ROIs. We will explore the influence of these (and other) nuisance effects on scan design in later subsections.

To isolate bias due to estimator nonlinearity from regularization bias, we minimize the ML initialization cost (S.1) only, and do not proceed to solve RLS problem (S.2). This permits consideration of T_1, T_2 estimation from each of the 7733 WM or 9384 GM data points as voxel-wise independent realizations of the same estimation problem. To minimize quantization bias, we optimize (S.1) using a very finely spaced dictionary of signal vectors from 1000 T_1 and T_2 values logarithmically spaced between $[10^2, 10^{3.5}]$ and $[10^1, 10^{2.5}]$, respectively. Using 10^6 dictionary elements, solving (S.1) took less than 7 minutes for each tested scan design \mathbf{P}^* .

Table II⁵ verifies that, despite model nonlinearity and Rician noise, estimation bias in WM- and GM-like voxels is negligible. Sample standard deviations are consistent with $\tilde{\sigma}_{T_1}^t$ and $\tilde{\sigma}_{T_2}^t$ (cf. Table I). In WM and GM, we observe that the (1, 1) and (0, 2) profiles afford high $\hat{\mathbf{T}}_1^{\text{ML}}$ precision, while the

⁵Each sample statistic presented hereafter is rounded off to the highest place value of its corresponding uncertainty measure. For simplicity, each uncertainty measure is itself endowed one extra significant figure. Decimal points indicate the significance of trailing zeros.

TABLE II

SAMPLE MEANS \pm SAMPLE STANDARD DEVIATIONS OF T_1 AND T_2 ML ESTIMATES IN WM AND GM ROIS OF SIMULATED DATA, COMPARED ACROSS DIFFERENT OPTIMIZED SCAN PROFILES. SAMPLE MEANS EXHIBIT INSIGNIFICANT BIAS, AND SAMPLE STANDARD DEVIATIONS ARE CONSISTENT WITH WORST-CASE STANDARD DEVIATIONS $\hat{\sigma}_{T_1}^t$ AND $\hat{\sigma}_{T_2}^t$ REPORTED IN

TABLE I. ALL VALUES ARE REPORTED IN MILLISECONDS

Scan	(2, 1)	(1, 1)	(0, 2)	Truth
WM \hat{T}_1^{ML}	830 \pm 17	830 \pm 15	830 \pm 14	832
GM \hat{T}_1^{ML}	1330 \pm 30.	1330 \pm 24	1330 \pm 24	1331
WM \hat{T}_2^{ML}	80. \pm 1.0	80. \pm 2.1	79.6 \pm 0.94	79.6
GM \hat{T}_2^{ML}	110. \pm 1.4	110. \pm 3.0	110. \pm 1.6	110

(2, 1) and (0, 2) scans afford high \hat{T}_2^{ML} precision. In agreement with the predictions of $\hat{\Psi}^t$ and $\hat{\Psi}^b$, these simulation studies suggest that at these SNR levels, an optimized profile containing 2 DESS scans can permit T_1 and T_2 estimation precision in WM and GM comparable to optimized profiles containing SPGR/DESS combinations.

B. Phantom Experiments

This subsection describes two experiments. In the first experiment, we compare the SPGR/DESS scan profiles described in Table I (as well as a reference profile consisting of IR and SE scans) against nuclear magnetic resonance (NMR) measurements from the National Institute for Standards and Technology (NIST) [68]. These measurements provide information about *ROI sample means* and *ROI sample standard deviations* (Fig. 1), which we define as first- and second-order statistics computed across voxels within an ROI. In the second experiment, we repeat the SPGR/DESS scan profiles 10 times and compute *sample standard deviation maps* across repetitions (not shown). Taking ROI sample means of these maps gives *pooled sample standard deviations* (Table III), which indicate relative scan profile precision.

1) Within-ROI Statistics: We acquire combinations of (2, 1), (1, 1), and (0, 2) SPGR and DESS coronal scans of a High Precision Devices[®] MR system phantom T_2 array. For each scan profile, we prescribe the optimized flip angles $\hat{\alpha}_0$ and repetition times \hat{T}_R listed in Table I, and hold all other scan parameters fixed. We achieve the desired nominal flip angles by scaling a 20 mm slab-selective Shinnar-Le Roux excitation [69], of duration 1.28 ms and time-bandwidth product 4. For each DESS (SPGR) scan, we apply 2 (10) spoiling phase cycles over a 5 mm slice thickness. We acquire all steady-state phantom and *in vivo* datasets with a $256 \times 256 \times 8$ matrix over a $240 \times 240 \times 30$ mm³ field of view (FOV). Using a 31.25 kHz readout bandwidth, we acquire all data at minimum $T_E \leftarrow 4.67\text{ms}$ before or after RF excitations. To avoid slice-profile effects, we sample \mathbf{k} -space over a 3D Cartesian grid. After Fourier transform of the raw datasets, only one of the excited image slices is used for subsequent parameter mapping. Including time to reach steady-state, each steady-state scan profile requires 1 m 37s scan time.

To validate a reference scan profile for use in *in vivo* experiments, we also collect 4 IR and 4 SE scans. For (phase-sensitive, SE) IR, we hold $(T_R, T_E) \leftarrow (1400, 14)\text{ms}$ fixed and vary (adiabatic) inversion time $T_1 \in \{50, 150, 450, 1350\}\text{ms}$ across scans. For SE, we similarly hold $T_R \leftarrow 1000\text{ms}$ fixed and vary echo time $T_E \in \{10, 30, 60, 150\}\text{ms}$ across scans. We prescribe these scan parameters to acquire 256×256 datasets over the same $240 \times 240 \times 5$ mm³ slice processed from the SPGR/DESS datasets. Each IR and SE scan requires 5 m 58 s and 4 m 16 s, for a total 40 m 58 s scan time.

We additionally collect a pair of Bloch-Siebert shifted 3D SPGR scans for separate B_1^+ estimation [70]. We insert a 9 ms Fermi pulse (peak amplitude $B_1^{\text{pk}} \leftarrow 0.075\text{G}$) at ± 8 kHz off-resonance into an SPGR sequence immediately following on-resonant excitation. We estimate regularized \hat{B}_1^+ maps [71] from the resulting pair of datasets. We then estimate flip angle variation $\hat{\kappa}$ as $\hat{B}_1^+ / B_1^{\text{pk}}$, calibrate $\hat{\kappa}$ (via separate measurements described in Section S.IV), and thereafter take κ as known. For consistency, we account for flip angle variation when estimating T_1 and T_2 from both the candidate (SPGR/DESS) and reference (IR/SE) aforementioned scan profiles. With a repetition time of 21.7 ms, this B_1^+ mapping acquisition requires 1 m 40 s total scan time.

Fig. 1 plots sample means and sample standard deviations computed within circular ROIs of phantom T_1 and T_2 ML estimates (reconstruction details, analogous plots for RLS estimates, and images in Sections S.V.A-S.V.C). The highlighted orange and yellow parameter spaces correspond to design ranges \mathcal{X}_i and \mathcal{X}_b . T_1 estimates from both the candidate (2, 1), (1, 1), and (0, 2) (SPGR, DESS) and reference (4, 4) (IR, SE) profiles are in reasonable agreement with NIST estimates [68] across the vial range. T_2 estimates from all profiles are also in good agreement with NIST for vials within \mathcal{X}_b . SPGR/DESS profiles likely underestimate large T_2 values ($\geq 200\text{ms}$) due to greater influence of diffusion in DESS [59]–[61]. SPGR/DESS profiles possibly overestimate and the IR/SE profile likely underestimates short ($\leq 30\text{ms}$) and very short ($\leq 15\text{ms}$) T_2 values, respectively, due to poorly conditioned estimation.

2) Across-Repetition Statistics: In a second study, we repeat the (2, 1), (1, 1), and (0, 2) scan profiles 10 times each and separately estimate T_1 and T_2 for each repetition of each scan profile. We then estimate the standard deviation across repetitions on a per-voxel basis, to produce sample standard deviation maps for each profile. Each ROI voxel of the sample standard deviation map is a better estimate of the *population standard deviation* (which the CRB characterizes) than the ROI sample standard deviation from a single repetition, because the latter estimate is contaminated with slight spatial variation of voxel population means (due to imaging non-idealities such as Gibbs ringing due to \mathbf{k} -space truncation).

Table III reports pooled sample standard deviations and pooled standard errors of the sample standard deviations (computed via expressions in [72]) for phantom vials within (or nearly within) tight design range \mathcal{X}_i (marked orange in Fig. S.7). Due to error propagation from coil combination and $\hat{\kappa}$ estimation, pooled ML sample standard deviations cannot be compared *in magnitude* to worst-case predicted

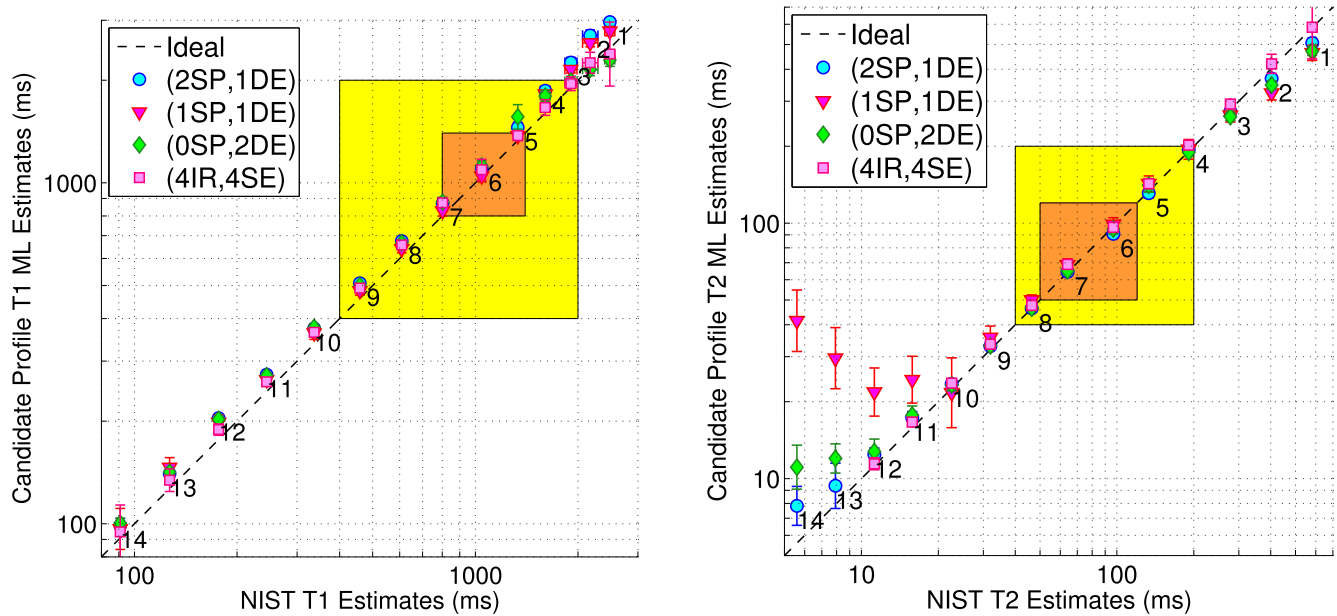


Fig. 1. Phantom within-ROI sample statistics of T_1 and T_2 ML estimates from optimized SPGR/DESS and reference IR/SE scan profiles vs. NIST NMR measurements [68]. Markers and error bars indicate ROI sample means and ROI sample standard deviations within the 14 labeled and color-coded vials in Fig. S.7. Tight \mathcal{X}_t and broad \mathcal{X}_b latent parameter ranges are highlighted in orange and yellow, respectively. Fig. S.8 provides analogous plots for RLS estimates. Table S.2 replicates sample statistics within Vials 5-8. Our MR measurements are at 293K, while NIST NMR measurements are at 293.00K. Within the designed parameter ranges, estimates from different acquisitions are in reasonable agreement with NIST measurements.

TABLE III

PHANTOM POOLED SAMPLE STANDARD DEVIATIONS \pm POOLED STANDARD ERRORS OF SAMPLE STANDARD DEVIATIONS, FROM OPTIMIZED SPGR/DESS SCAN PROFILES. EACH ENTRY IS A MEASURE OF UNCERTAINTY OF A TYPICAL VOXEL'S T_1 OR T_2 ML ESTIMATE. FOR SAKE OF BREVITY, SAMPLE STATISTICS CORRESPONDING ONLY TO PHANTOM VIALS WITHIN (OR NEARLY WITHIN) TIGHT DESIGN RANGE \mathcal{X}_t (COLOR-CODED ORANGE IN Fig. S.7) ARE REPORTED. 'V#' ABBREVIATES VIAL NUMBERS. ALL VALUES ARE REPORTED IN MILLISECONDS

	(2SP,1DE)	(1SP,1DE)	(0SP,2DE)		(2SP,1DE)	(1SP,1DE)	(0SP,2DE)
V5 $\hat{\sigma}_{\hat{T}_1 \text{ML}}(\mathbf{P}^*)$	50 \pm 12	40 \pm 10.	39 \pm 9.4	V5 $\hat{\sigma}_{\hat{T}_2 \text{ML}}(\mathbf{P}^*)$	2.6 \pm 0.63	6 \pm 1.4	3.5 \pm 0.84
V6 $\hat{\sigma}_{\hat{T}_1 \text{ML}}(\mathbf{P}^*)$	70 \pm 18	60 \pm 15	70 \pm 16	V6 $\hat{\sigma}_{\hat{T}_2 \text{ML}}(\mathbf{P}^*)$	1.9 \pm 0.46	5 \pm 1.1	2.3 \pm 0.54
V7 $\hat{\sigma}_{\hat{T}_1 \text{ML}}(\mathbf{P}^*)$	60 \pm 13	50 \pm 13	50 \pm 13	V7 $\hat{\sigma}_{\hat{T}_2 \text{ML}}(\mathbf{P}^*)$	1.4 \pm 0.34	3.4 \pm 0.80	1.5 \pm 0.35
V8 $\hat{\sigma}_{\hat{T}_1 \text{ML}}(\mathbf{P}^*)$	23 \pm 5.4	20. \pm 4.7	18 \pm 4.3	V8 $\hat{\sigma}_{\hat{T}_2 \text{ML}}(\mathbf{P}^*)$	1.1 \pm 0.26	3.5 \pm 0.84	1.4 \pm 0.33

standard deviations (Table I); however, *trends* of empirical and theoretical standard deviations are overall similar. In particular, the optimized (0, 2) DESS-only scan profile affords T_1 ML estimation precision (in vials whose T_1, T_2 is similar to that of WM/GM) comparable to optimized (2, 1) and (1, 1) mixed (SPGR, DESS) profiles. Also in agreement with predictions, the optimized (2, 1) and (0, 2) profiles afford greater T_2 ML estimation precision than the optimized (1, 1) profile.

C. In Vivo Experiments

In a single long study of a healthy volunteer, we acquire the same optimized scan profiles containing (2, 1), (1, 1), and (0, 2) SPGR and DESS scans (*cf.* Table I), as well as the reference profile containing (4, 4) IR and SE scans. We obtain axial slices from a 32-channel Nova Medical® receive head array. To address bulk motion between acquisitions and to compare within-ROI statistics, we rigidly register each coil-combined image to an IR image (details in Section S.V.D)

prior to parameter mapping. All acquisition (*cf.* Section IV-B.1) and reconstruction (*cf.* Sections S.V.A-S.V.B) details are otherwise the same as in phantom experiments.

Fig. 2 compares brain T_1 and T_2 ML estimates from optimized scan profiles (Fig. S.9 and Fig. S.10 provide corresponding colorized and grayscale RLS estimates, respectively). Though in-plane motion is largely compensated via registration, through-plane motion and non-bulk motion likely persist, and will influence ROI statistics. Due to motion (and scan duration) considerations, we examine within-ROI statistics from a single repetition as in Section IV-B.1, and do not attempt across-repetition statistics as in Section IV-B.2.

Visually, \hat{T}_1 maps from steady-state profiles exhibit similar levels of contrast in WM/GM regions well away from cerebrospinal fluid (CSF) as that seen in the reference \hat{T}_1 estimate. Since we did not optimize any scan profiles for estimation in high- T_1 regions, it is expected that greater differences may emerge in voxels containing or nearby CSF. In particular,

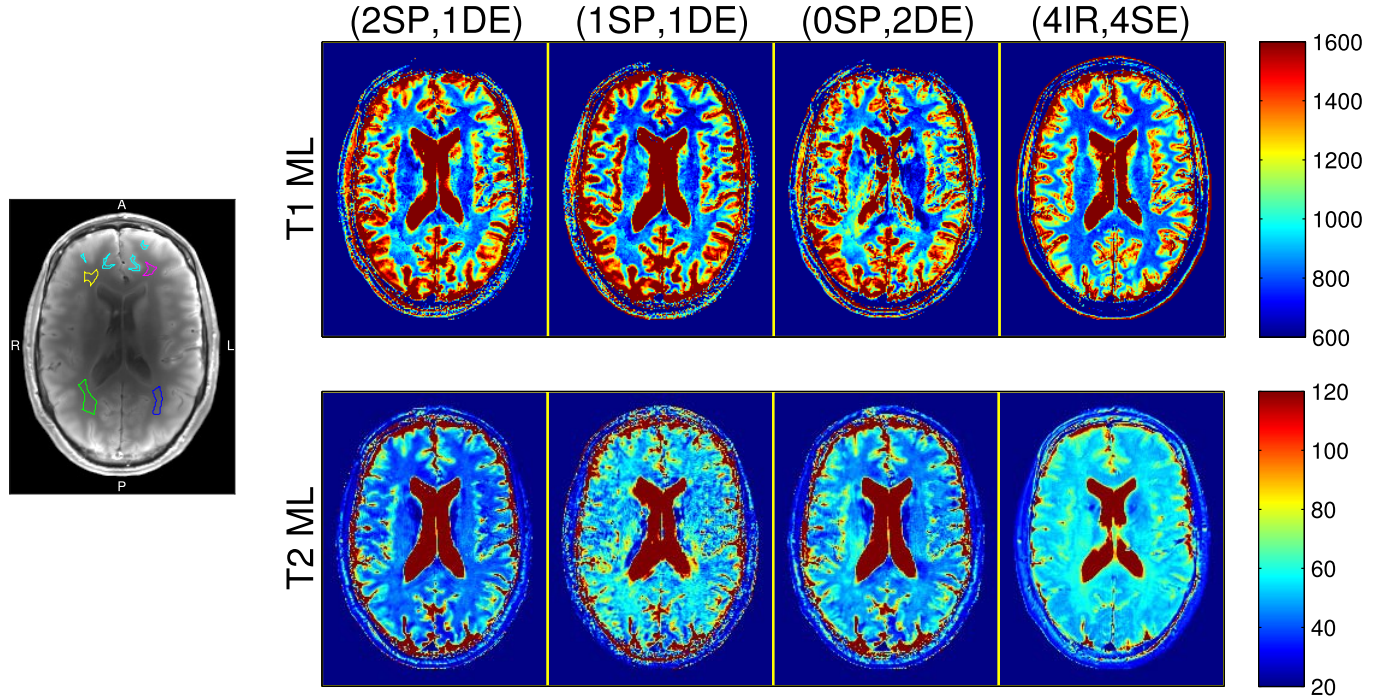


Fig. 2. Left: WM and GM ROIs, overlaid on a representative anatomical (coil-combined IR) image. Separate WM ROIs are distinguished with anterior/posterior (A/P) and right/left (R/L) directions. Four small anterior cortical GM polygons are pooled into a single ROI (cyan). Right: Colorized T_1 and T_2 ML estimates from the brain of a healthy volunteer. Columns correspond to profiles consisting of (2 SPGR, 1 DESS), (1 SPGR, 1 DESS), (0 SPGR, 2 DESS), and (4 IR, 4 SE) acquisitions. Parameter maps are cropped in post-processing for the purpose of display. Figs. S.9 (colorized) and S.10 (grayscale) provide analogous full-FOV maps estimated via both ML and RLS estimators. Colorbar ranges are in milliseconds.

T_1 is significantly underestimated within and near CSF by the (0, 2) DESS-only profile. This suggests that with the signal models used in this work, including at least one SPGR scan in an optimized profile may offer greater protection against estimation bias in high- T_1 regions.

Table IV summarizes within-ROI sample means and sample standard deviations computed⁶ over four separate WM ROIs containing 96, 69, 224, and 148 voxels and one pooled cortical GM ROI containing 156 voxels (cf. Fig. 2). Within-ROI \hat{T}_1 sample standard deviations are comparable across steady-state profiles. In agreement with Table I, T_2 estimates from the optimized (1, 1) scan profile exhibit higher within-ROI sample variation than corresponding (2, 1) and (0, 2) \hat{T}_2 maps.

In most cases, \hat{T}_1 within-ROI sample means from optimized SPGR/DESS scan profiles do not deviate substantially from each other or from reference IR/SE measurements. Two notable exceptions are \hat{T}_1^{ML} in anterior left and posterior right WM from (1, 1) and (0, 2) profiles: these estimates are significantly lower and higher than analogous estimates from other profiles, respectively. Results thus suggest that the optimized (2, 1) scan profile yields WM \hat{T}_1^{ML} estimates that are more consistently similar to IR WM \hat{T}_1^{ML} estimates than other optimized SPGR/DESS profiles.

⁶We have taken effort to try and select ROIs that reflect expected anatomy in all coil-combined and registered images, including adjacent slices in images from 3D acquisitions. However, we acknowledge the possibility of some contamination across tissue boundaries, especially WM and/or CSF contamination into cortical GM.

Systematic differences in \hat{T}_2 sample means are evident across scan profiles, particularly within WM ROIs. Curiously, the (1, 1) profile agrees most consistently (in WM/GM \hat{T}_2^{ML} within-ROI sample mean) with reference estimates, though with relatively high sample variation. The (2, 1) and (0, 2) SPGR/DESS profiles produce consistently lower WM \hat{T}_2^{ML} than the reference IR/SE profile, though the (0, 2) profile is in reasonable agreement with other steady-state estimates [73]. These discrepancies may be due to differences in sensitivity to multi-compartmental relaxation [74]. Specifically, different signal models with different scan parameter choices might be more or less sensitive to the model mismatch incurred by neglecting to distinguish the multiple T_2 components within each voxel. Section S.VI studies T_2 estimation bias due to multi-compartmental relaxation in more detail.

V. DISCUSSION AND FUTURE WORK

Phantom experiments show that optimized scan profiles consisting of (2, 1), (1, 1), and (0, 2) (SPGR, DESS) scans yield accurate WM/GM T_1, T_2 estimates, and that empirical precision trends across profiles agree reasonably with CRB-based predictions. However, *in vivo* experiments reveal that even with scan optimization, it may be challenging to achieve clinically viable levels of precision from the aforementioned steady-state profiles, at least at 3T. At the expense of greater scan time, it is of course possible that optimized profiles containing greater numbers of SPGR, DESS, and/or other steady-state scans can provide clinically acceptable precision

TABLE IV

WITHIN-ROI SAMPLE MEANS \pm WITHIN-ROI SAMPLE STANDARD DEVIATIONS OF T_1 AND T_2 ML ESTIMATES FROM THE BRAIN OF A HEALTHY VOLUNTEER. SAMPLE STATISTICS ARE COMPUTED WITHIN ROIS INDICATED IN FIG. 2. ALL VALUES ARE REPORTED IN MILLISECONDS

	ROI (color)	(2SP,1DE)	(1SP,1DE)	(0SP,2DE)	(4IR,4SE)
\hat{T}_1^{ML}	anterior right WM (yellow)	840 \pm 32	770 \pm 31	840 \pm 43	780 \pm 22
	anterior left WM (magenta)	740 \pm 61	660 \pm 45	740 \pm 55	760 \pm 24
	posterior right WM (green)	890 \pm 88	860 \pm 72	960 \pm 84	810 \pm 26
	posterior left WM (blue)	860 \pm 70.	850 \pm 61	880 \pm 79	820 \pm 37
	anterior GM (cyan)	1200 \pm 210	1200 \pm 230	1300 \pm 230	1300 \pm 180
\hat{T}_2^{ML}	anterior right WM (yellow)	40. \pm 1.3	54 \pm 3.8	46 \pm 1.5	55 \pm 1.9
	anterior left WM (magenta)	40. \pm 1.7	50. \pm 4.5	44 \pm 1.7	53 \pm 1.8
	posterior right WM (green)	43 \pm 2.7	60. \pm 6.9	51 \pm 3.6	59 \pm 2.1
	posterior left WM (blue)	43 \pm 1.8	57 \pm 4.9	49 \pm 2.5	57 \pm 1.8
	anterior GM (cyan)	50 \pm 12	60 \pm 15	60 \pm 11	59 \pm 6.0

levels. For these and other more complicated scan profiles, estimator dependence on scan parameters becomes even less intuitive, increasing the need for scan design.

The proposed scan design framework addresses spatial variation in object parameters through a min-max design criterion. The min-max criterion guarantees an upper bound on a weighted sum of variances and assumes no prior knowledge of distributions. However, in general it is non-differentiable in \mathbf{P} , precluding gradient-based optimization. Furthermore, it is conservative by nature, and often selects scan parameters based on corner cases of the object parameter space. To reduce the influence of corner cases, it may be desirable to instead construct a cost function related to the coefficient of variation as in [44], [46]–[48], perhaps by setting parameter weights $\mathbf{W}^{-1} \leftarrow \text{diag}(\mathbf{x})$ for $\mathbf{x} \neq 0$ in (5).

As a less conservative alternative to min-max design, other recent works [50], [51] have addressed object parameter spatial variation by instead constructing cost functions related to the Bayesian CRB [75], which characterizes the expected precision with respect to a prior distribution on object parameters. Bayesian cost functions are usually differentiable and can also, with appropriate priors, penalize object parameter coefficients of variation instead of variances, as in [50]. However, prior distributions are generally unknown, and may need to be estimated from data, as in [51].

Careful calibration of flip angle scaling κ is essential for accurate T_1 , T_2 estimation from SPGR/DESS scan profiles. In this work, we estimate κ from *separate* acquisitions and adjust nominal flip angles prior to reconstruction, but acknowledge that non-idealities in those separate acquisitions may themselves cause resultant $\hat{\mathbf{B}}_1^+$ errors to propagate into our T_1 , T_2 estimates. To reduce error propagation, it may be desirable to instead design scan profiles to permit *joint* estimation of κ , in addition to other latent object parameters. Unfortunately, we find that optimizing the (2, 1) or (0, 2) profile to allow for four-parameter $\mathbf{x}(\mathbf{r}) := [M_E(\mathbf{r}), T_1(\mathbf{r}), T_2(\mathbf{r}), \kappa(\mathbf{r})]^T$ estimation results in unacceptably high amplification of the worst-case T_1 standard deviation. (Incidentally, precise T_2 ML and RLS estimation alone from the (2, 1) or (0, 2) profile is possible [42].) It remains an open scan design question as to whether time spent collecting Bloch-Siegert data for separate \mathbf{B}_1^+ mapping could instead be better spent collecting additional SPGR, DESS, and/or other data for joint estimation.

By working with closed-form signal expressions, we neglect to model several higher-order effects. However, it is apparent

that the nonlinear estimation procedures required for many mapping problems can amplify the influence of these secondary effects, often inducing substantial bias. Since the CRB (as described) applies only to unbiased estimators, it is thus desirable to use signal models that are as complete as possible for CRB-based scan design. In theory, scan optimization approach (9) is even compatible with acquisitions where a closed-form model relating data to latent and scan parameters is unknown, as in [22], [76]. In practice, difficulties arise in efficient computation of signal gradients required in (3), which may demand more specialized techniques, as in [77]. Designing scan profiles involving such complex signal models would likely necessitate optimization techniques more involved than the simple grid searches used in this work.

VI. CONCLUSION

We have introduced a CRB-inspired min-max optimization approach to aid robust, application-specific MR scan selection and optimization for precise parameter estimation. As a detailed example, we have optimized combinations of fast SPGR and DESS scans for T_1 , T_2 relaxometry in WM and GM regions of the human brain at 3T. Numerical simulations show that at typical noise levels and with accurate flip angle prior knowledge, WM- and GM-like T_1 , T_2 ML estimates from optimized scans are nearly unbiased, and so worst-case CRB predictions yield reliable bounds on ROI sample variances. Phantom accuracy experiments show that optimized combinations of (2, 1), (1, 1), or (0, 2) (SPGR, DESS) scans are in excellent agreement with NIST and IR/SE measurements over the designed latent object parameter range of interest. Phantom precision experiments show that these SPGR/DESS combinations exhibit trends in pooled sample standard deviations that reasonably reflect CRB predictions.

In vivo experiments suggest that with optimization, the (0, 2) profile can yield comparable \hat{T}_1 , \hat{T}_2 precision to the more conventional (2, 1) [42] scan profile in well-isolated WM/GM ROIs; however, the (0, 2) T_1 estimates are unreliable within and near the CSF and do not agree with IR measurements in WM as consistently as the (2, 1) profile. This and other disagreements across profiles *in vivo* may be attributable to differences in signal model sensitivities to neglected higher-order effects. Nevertheless, this simple example application illustrates that scan optimization may enable new parameter mapping techniques from established pulse sequences.

ACKNOWLEDGEMENT

The authors thank Dr. Kathryn Keenan and Dr. Stephen Russek at NIST for generously lending a prototype [78] (used in initial experiments) of the High Precision Devices® MR system phantom, and for sharing an early preprint of [68]. The authors also thank the reviewers for their helpful suggestions.

REFERENCES

- [1] H.-L. M. Cheng, N. Stikov, N. R. Ghugre, and G. A. Wright, "Practical medical applications of quantitative MR relaxometry," *J. Mag. Reson. Imag.*, vol. 36, no. 4, pp. 805–824, Oct. 2012.
- [2] H. B. W. Larsson, J. Frederiksen, L. Kjaer, O. Henriksen, and J. Olesen, "In vivo determination of T_1 and T_2 in the brain of patients with severe but stable multiple sclerosis," *Mag. Reson. Med.*, vol. 7, no. 1, pp. 43–55, May 1988.
- [3] T. Kurki, N. Lundbom, M. Komu, and M. Korman, "Tissue characterization of intracranial tumors by magnetization transfer and spin-lattice relaxation parameters in vivo," *J. Mag. Reson. Imag.*, vol. 6, no. 4, pp. 573–579, Aug. 1996.
- [4] E. Englund, A. Brun, Z. G. Wagner, E. Larsson, and B. Persson, "Relaxation times in relation to grade of malignancy and tissue necrosis in astrocytic gliomas," *Mag. Reson. Imag.*, vol. 4, no. 5, pp. 425–429, 1986.
- [5] S. Siemensen *et al.*, "Quantitative T_2 values predict time from symptom onset in acute stroke patients," *Stroke*, vol. 40, no. 5, pp. 1612–1616, Apr. 2009.
- [6] L. D. DeWitt, J. P. Kistler, D. C. Miller, E. P. Richardson, and F. S. Buonanno, "NMR-neuropathologic correlation in stroke," *Stroke*, vol. 18, no. 2, pp. 342–351, Mar. 1987.
- [7] S. J. Matzat, J. V. Tiel, G. E. Gold, and E. H. G. Oei, "Quantitative MRI techniques of cartilage composition," *Quant. Imag. Med. Surg.*, vol. 3, no. 3, pp. 162–174, Jun. 2013.
- [8] T. J. Mosher and B. J. Dardzinski, "Cartilage MRI T_2 relaxation time mapping: Overview and applications," *Seminars Musculoskeletal Radiol.*, vol. 8, no. 4, pp. 355–368, Jan. 2005.
- [9] H. Guo *et al.*, "Myocardial T_2 quantification in patients with iron overload at 3 Tesla," *J. Magn. Reson. Imag.*, vol. 30, no. 2, pp. 394–400, Aug. 2009.
- [10] S. Giri *et al.*, " T_2 quantification for improved detection of myocardial edema," *J. Cardiovasc. Magn. Reson.*, vol. 11, no. 1, pp. 56–68, Dec. 2009.
- [11] D. C. Look and D. R. Locker, "Time saving in measurement of NMR and EPR relaxation times," *Rev. Sci. Instrum.*, vol. 41, no. 2, pp. 250–251, Feb. 1970.
- [12] H. Y. Carr and E. M. Purcell, "Effects of diffusion on free precession in nuclear magnetic resonance experiments," *Phys. Rev.*, vol. 94, no. 3, pp. 630–638, May 1954.
- [13] M. K. Stehling, R. Turner, and P. Mansfield, "Echo-planar imaging: Magnetic resonance imaging in a fraction of a second," *Science*, vol. 254, no. 5028, pp. 43–50, Oct. 1991.
- [14] C. B. Ahn, J. H. Kim, and Z. H. Cho, "High-speed spiral-scan echo planar NMR imaging-I," *IEEE Trans. Med. Imag.*, vol. 5, no. 1, pp. 2–7, Mar. 1986.
- [15] C. H. Meyer, B. S. Hu, D. G. Nishimura, and A. Macovski, "Fast spiral coronary artery imaging," *Mag. Reson. Med.*, vol. 28, no. 2, pp. 202–213, Dec. 1992.
- [16] I. Kay and R. M. Henkelman, "Practical implementation and optimization of one-shot T_1 imaging," *Mag. Reson. Med.*, vol. 22, no. 2, pp. 414–424, Dec. 1991.
- [17] P. A. Gowland and M. O. Leach, "Fast and accurate measurements of T_1 using a multi-readout single inversion-recovery sequence," *Mag. Reson. Med.*, vol. 26, no. 1, pp. 79–88, Jul. 1992.
- [18] D. R. Messroghli, A. Radjenovic, S. Kozerke, D. M. Higgins, M. U. Sivanathan, and J. P. Ridgway, "Modified Look-Locker inversion recovery (MOLLI) for high-resolution T_1 mapping of the heart," *Mag. Reson. Med.*, vol. 52, no. 1, pp. 141–146, Jul. 2004.
- [19] M. K. Stehling, R. J. Ordidge, R. Coxon, and P. Mansfield, "Inversion-recovery echo-planar imaging (IR-EPI) at 0.5T," *Mag. Reson. Med.*, vol. 13, no. 3, pp. 514–517, Mar. 1990.
- [20] J.-M. Bonny, M. Zanca, J.-Y. Boire, and A. Veyre, " T_2 maximum likelihood estimation from multiple spin-echo magnitude images," *Mag. Reson. Med.*, vol. 36, no. 2, pp. 287–293, Aug. 1996.
- [21] D. Kumar, T. D. Nguyen, S. A. Gauthier, and A. Raj, "Bayesian algorithm using spatial priors for multiexponential T_2 relaxometry from multiecho spin echo MRI," *Mag. Reson. Med.*, vol. 68, no. 5, pp. 1536–1543, Nov. 2012.
- [22] N. B. Eliezer, D. K. Sodickson, and K. T. Block, "Rapid and accurate T_2 mapping from multi-spin-echo data using Bloch-simulation-based reconstruction," *Mag. Reson. Med.*, vol. 73, no. 2, pp. 809–817, Feb. 2015.
- [23] T. D. Nguyen *et al.*, " T_2 prep three-dimensional spiral imaging with efficient whole brain coverage for myelin water quantification at 1.5 Tesla," *Mag. Reson. Med.*, vol. 67, no. 3, pp. 614–621, Mar. 2012.
- [24] S. Majumdar, S. C. Orphanoudakis, A. Gmitro, M. O'Donnell, and J. C. Gore, "Error in the measurements of T_2 using multiple-echo MRI techniques: 1. Effect of radiofrequency pulse imperfections," *Mag. Reson. Med.*, vol. 3, no. 3, pp. 397–417, Jun. 1986.
- [25] S. Majumdar, S. C. Orphanoudakis, A. Gmitro, M. O'Donnell, and J. C. Gore, "Error in the measurements of T_2 using multiple-echo MRI techniques: 2. Effects of static field inhomogeneity," *Mag. Reson. Med.*, vol. 3, no. 4, pp. 562–574, Aug. 1986.
- [26] F. Farzaneh, S. J. Riederer, and N. J. Pelc, "Analysis of T_2 limitations and off-resonance effects on spatial resolution and artifacts in echo-planar imaging," *Mag. Reson. Med.*, vol. 14, no. 1, pp. 123–139, Apr. 1990.
- [27] W. S. Hinshaw, "Image formation by nuclear magnetic resonance: The sensitive point method," *J. Appl. Phys.*, vol. 47, no. 8, p. 3709, Aug. 1976.
- [28] K. Scheffler, "A pictorial description of steady-states in rapid magnetic resonance imaging," *Concepts Magn. Reson.*, vol. 11, no. 5, pp. 291–304, Jul. 1999.
- [29] S. C. Deoni, B. K. Rutt, and T. M. Peters, "Rapid combined T_1 and T_2 mapping using gradient recalled acquisition in the steady state," *Mag. Reson. Med.*, vol. 49, no. 3, pp. 515–526, Mar. 2003.
- [30] L.-C. Chang, C. G. Koay, P. J. Basser, and C. Pierpaoli, "Linear least-squares method for unbiased estimation of T_1 from SPGR signals," *Mag. Reson. Med.*, vol. 60, no. 2, pp. 496–501, Aug. 2008.
- [31] E. K. Fram *et al.*, "Rapid calculation of T_1 using variable flip angle gradient refocused imaging," *Mag. Reson. Imag.*, vol. 5, no. 3, pp. 201–208, 1987.
- [32] H. Wang and Y. Cao, "Spatially regularized T_1 estimation from variable flip angles MRI," *Med. Phys.*, vol. 39, no. 7, pp. 4139–4148, Jul. 2012.
- [33] S. C. L. Deoni, H. A. Ward, T. M. Peters, and B. K. Rutt, "Rapid T_2 estimation with phase-cycled variable nutation steady-state free precession," *Mag. Reson. Med.*, vol. 52, no. 2, pp. 435–439, Aug. 2004.
- [34] S. C. L. Deoni, "Transverse relaxation time (T_2) mapping in the brain with off-resonance correction using phase-cycled steady-state free precession imaging," *J. Mag. Reson. Imag.*, vol. 30, no. 2, pp. 411–417, Aug. 2009.
- [35] G. H. Welsch *et al.*, "Rapid estimation of cartilage T_2 based on double echo at steady state (DESS) with 3 Tesla," *Mag. Reson. Med.*, vol. 62, no. 2, pp. 544–549, Aug. 2009.
- [36] R. Heule, C. Ganter, and O. Bieri, "Rapid estimation of cartilage T_2 with reduced T_1 sensitivity using double echo steady state imaging," *Mag. Reson. Med.*, vol. 71, no. 3, pp. 1137–1143, Mar. 2014.
- [37] T. Stöcker, F. Keil, K. Vahedipour, D. Brenner, E. Pracht, and N. J. Shah, "MR parameter quantification with magnetization-prepared double echo steady-state (MP-DESS)," *Mag. Reson. Med.*, vol. 72, no. 1, pp. 103–111, Jul. 2014.
- [38] R. Heule, C. Ganter, and O. Bieri, "Triple echo steady-state (TESS) relaxometry," *Mag. Reson. Med.*, vol. 71, no. 1, pp. 230–237, Jan. 2014.
- [39] H. Bruder, H. Fischer, R. Graumann, and M. Deimling, "A new steady-state imaging sequence for simultaneous acquisition of two MR images with clearly different contrasts," *Mag. Reson. Med.*, vol. 7, no. 1, pp. 35–42, May 1988.
- [40] M. L. Gyngell, "The steady-state signals in short-repetition-time sequences," *J. Mag. Reson.*, vol. 81, no. 3, pp. 474–483, Feb. 1989.
- [41] W. Hänicke and H. U. Vogel, "An analytical solution for the SSFP signal in MRI," *Mag. Reson. Med.*, vol. 49, no. 4, pp. 771–775, Apr. 2003.

- [42] G. Nataraj, J.-F. Nielsen, and J. A. Fessler, "Model-based estimation of T_2 maps with dual-echo steady-state MR imaging," in *Proc. IEEE Int. Conf. Image Process.*, Oct. 2014, pp. 1877–1881.
- [43] G. H. Weiss, R. K. Gupta, J. A. Ferretti, and E. D. Becker, "The choice of optimal parameters for measurement of spin-lattice relaxation times. I. Mathematical formulation," *J. Mag. Reson.*, vol. 37, no. 3, pp. 369–379, Feb. 1980.
- [44] Y. Zhang, H. N. Yeung, M. O'Donnell, and P. L. Carson, "Determination of sample time for T_1 measurement," *J. Mag. Reson. Imag.*, vol. 8, no. 3, pp. 675–681, May 1998.
- [45] H. Z. Wang, S. J. Riederer, and J. N. Lee, "Optimizing the precision in T_1 relaxation estimation using limited flip angles," *Mag. Reson. Med.*, vol. 5, no. 5, pp. 399–416, Nov. 1987.
- [46] J. A. Jones, P. Hodgkinson, A. L. Barker, and P. J. Hore, "Optimal sampling strategies for the measurement of spin-spin relaxation times," *J. Mag. Reson. B*, vol. 113, no. 1, pp. 25–34, Oct. 1996.
- [47] J. Imran, F. Langevin, and H. S. Jalmes, "Two-point method for T_1 estimation with optimized gradient-echo sequence," *Mag. Reson. Imag.*, vol. 17, no. 9, pp. 1347–1356, Nov. 1999.
- [48] S. C. L. Deoni, T. M. Peters, and B. K. Rutt, "Determination of optimal angles for variable nutation proton magnetic spin-lattice, T_1 , and spin-spin, T_2 , relaxation times measurement," *Mag. Reson. Med.*, vol. 51, no. 1, pp. 194–199, Jan. 2004.
- [49] L. Fleysheer, R. Fleysheer, S. Liu, W. Zaaaroui, and O. Gonen, "Optimizing the precision-per-unit-time of quantitative MR metrics: Examples for T_1 , T_2 , and DTI," *Mag. Reson. Med.*, vol. 57, no. 2, pp. 380–387, Feb. 2007.
- [50] M. Akçakaya, S. Weingärtner, S. Roujol, and R. Nezafat, "On the selection of sampling points for myocardial T_1 mapping," *Mag. Reson. Med.*, vol. 73, no. 5, pp. 1741–1753, May 2015.
- [51] C. M. Lewis, S. A. Hurley, M. E. Meyerand, and C. G. Koay, "Data-driven optimized flip angle selection for T_1 estimation from spoiled gradient echo acquisitions," *Mag. Reson. Med.*, vol. 76, no. 3, pp. 792–802, Sep. 2016.
- [52] J. A. Fessler and B. P. Sutton, "Nonuniform fast Fourier transforms using min-max interpolation," *IEEE Trans. Signal Proc.*, vol. 51, no. 2, pp. 560–574, Feb. 2003.
- [53] M. J. Muckley, D. C. Noll, and J. A. Fessler, "Fast parallel MR image reconstruction via B1-based, adaptive restart, iterative soft thresholding algorithms (BARISTA)," *IEEE Trans. Med. Imag.*, vol. 34, no. 2, pp. 578–588, Feb. 2015.
- [54] A. Macovski, "Noise in MRI," *Mag. Reson. Med.*, vol. 36, no. 3, pp. 494–497, Sep. 1996.
- [55] T. Lei, "Statistics of MR signals: revisited," in *Proc. SPIE*, Mar. 2007, p. 651052.
- [56] R. A. Fisher, "Theory of statistical estimation," *Proc. Cambridge Phil. Soc.*, vol. 22, no. 5, pp. 700–725, Jul. 1925.
- [57] H. Cramer, *Mathematical Methods of Statistics*. Princeton, NJ, USA: Princeton Univ. Press, 1946.
- [58] H. Chernoff, "Locally optimal designs for estimating parameters," *Annu. Math. Statist.*, vol. 24, no. 4, pp. 586–602, Dec. 1953. [Online]. Available: <http://www.jstor.org/stable/2236782>
- [59] C. E. Carney, S. T. S. Wong, and S. Patz, "Analytical solution and verification of diffusion effect in SSFP," *Mag. Reson. Med.*, vol. 19, no. 2, pp. 240–246, Jun. 1991.
- [60] E. X. Wu and R. B. Buxton, "Effect of diffusion on the steady-state magnetization with pulsed field gradients," *J. Mag. Reson.*, vol. 90, no. 2, pp. 243–253, Nov. 1990.
- [61] R. Kaiser, E. Bartholdi, and R. R. Ernst, "Diffusion and field-gradient effects in NMR Fourier spectroscopy," *J. Chem. Phys.*, vol. 60, no. 8, pp. 2966–2979, Apr. 1974.
- [62] O. Bieri and K. Scheffler, "SSFP signal with finite RF pulses," *Mag. Reson. Med.*, vol. 62, no. 5, pp. 1232–1241, Nov. 2009.
- [63] Y. Zur, M. L. Wood, and L. J. Neuringer, "Spoiling of transverse magnetization in steady-state sequences," *Mag. Reson. Med.*, vol. 21, no. 2, pp. 251–263, Oct. 1991.
- [64] J. P. Wansapura, S. K. Holland, R. S. Dunn, and W. S. Ball, "NMR relaxation times in the human brain at 3.0 Tesla," *J. Mag. Reson.*, vol. 9, no. 4, pp. 531–538, Apr. 1999.
- [65] G. J. Stanisz *et al.*, " T_1 , T_2 relaxation and magnetization transfer in tissue at 3T," *Mag. Reson. Med.*, vol. 54, no. 3, pp. 507–512, Sep. 2005.
- [66] R. K.-S. Kwan, A. C. Evans, and G. B. Pike, "MRI simulation-based evaluation of image-processing and classification methods," *IEEE Trans. Med. Imag.*, vol. 18, no. 11, pp. 1085–1097, Nov. 1999.
- [67] D. L. Collins *et al.*, "Design and construction of a realistic digital brain phantom," *IEEE Trans. Med. Imag.*, vol. 17, no. 3, pp. 463–468, Jun. 1998.
- [68] K. E. Keenan *et al.*, "Multi-site, multi-vendor comparison of T_1 measurement using ISMRM/NIST system phantom," in *Proc. Int. Soc. Mag. Reson. Med.*, 2016, p. 3290.
- [69] J. Pauly, P. Le Roux, D. Nishimura, and A. Macovski, "Parameter relations for the Shinnar-Le Roux selective excitation pulse design algorithm," *IEEE Trans. Med. Imag.*, vol. 10, no. 1, pp. 53–65, Mar. 1991.
- [70] L. I. Sacolick, F. Wiesinger, I. Hancu, and M. W. Vogel, "B1 mapping by Bloch-Siegert shift," *Mag. Reson. Med.*, vol. 63, no. 5, pp. 1315–1322, May 2010.
- [71] H. Sun, W. A. Grissom, and J. A. Fessler, "Regularized estimation of Bloch-Siegert $|B_1^+|$ maps in MRI," in *Proc. IEEE Int. Conf. Image Process.*, Oct. 2014, pp. 3646–3650.
- [72] S. Ahn and J. A. Fessler, "Standard errors of mean, variance, and standard deviation estimators," Dept. EECS, Univ. Michigan, Ann Arbor, MI, USA: Tech. Rep. 413, Jul. 2003.
- [73] R. Heule, P. Bär, C. Mirkes, K. Scheffler, S. Trattnig, and O. Bieri, "Triple-echo steady-state T_2 relaxometry of the human brain at high to ultra-high fields," *NMR Biomed.*, vol. 27, no. 9, pp. 1037–1045, Sep. 2014.
- [74] A. Mackay, K. Whittall, J. Adler, D. Li, D. Paty, and D. Graeb, "In vivo visualization of myelin water in brain by magnetic resonance," *Mag. Reson. Med.*, vol. 31, no. 6, pp. 673–677, Jun. 1994.
- [75] R. D. Gill and B. Y. Levit, "Applications of the van Trees inequality: A Bayesian Cramér-Rao bound," *Bernoulli*, vol. 1, nos. 1–2, pp. 59–79, 1995. [Online]. Available: <http://www.jstor.org/stable/3318681>
- [76] D. Ma *et al.*, "Magnetic resonance fingerprinting," *Nature*, vol. 495, pp. 187–193, Mar. 2013.
- [77] B. Zhao, J. Haldar, K. Setsompop, and L. L. Wald, "Optimal experiment design for magnetic resonance fingerprinting," in *Proc. 38th Annu. Int. Conf. IEEE Eng. Med. Biol. Soc.*, 2016, pp. 453–456.
- [78] S. E. Russek *et al.*, "Characterization of NIST/ISMRM MRI system phantom," in *Proc. Int. Soc. Mag. Reson. Med.*, 2012, p. 2456. [Online]. Available: <http://cds.ismrm.org/protected/12MProceedings/files/2456>

Supplementary Material for Optimizing MR Scan Design for Model-Based T_1, T_2 Estimation from Steady-State Sequences

G. Nataraj^{*}, J. F. Nielsen[†], and J. A. Fessler^{*}

^{*}Dept. of Electrical Engineering and Computer Science, University of Michigan

[†]Dept. of Biomedical Engineering, University of Michigan

This supplement elaborates upon methodology details and presents additional figures that could not be included in the Manuscript [1] due to page restrictions. Section S.I provides visualizations of scan parameter optimization problem (9) in the Manuscript and relates min-max scan design to prior art. Section S.II describes methods for latent object parameter estimation from optimized scan profiles. Section S.III presents images and histograms corresponding to Manuscript Section IV.A. Section S.V elaborates upon image reconstruction and parameter estimation details for phantom and *in vivo* experiments (Manuscript Sections IV.B-IV.C). Lastly, Section S.VI explores the effect of model mismatch due to multi-exponential relaxation on single-component T_2 estimation.

S.I Optimized Scan Design: Further Details

S.I.A Scan Profile Comparisons

Fig. S.1 displays heat maps of worst-case latent parameter standard deviations $\tilde{\sigma}_{T_1}^t$, $\tilde{\sigma}_{T_2}^t$ and worst-case cost $\tilde{\Psi}^t$ as pairs of flip angles are varied away from the optimized scan design \mathbf{P}^* . When present hereafter, boxes group subfigures corresponding to the same scan profile. Viewing the bottom row of subfigures, it is evident that $\tilde{\Psi}^t(\mathbf{P}^*)$ takes similar values for the different scan profiles. However, it is apparent that the $(C_{\text{SPGR}}, C_{\text{DESS}}) = (0, 2)$ profile is substantially more robust to flip angle variation than other tested profiles (namely, $(2, 1)$ and $(1, 1)$). Optimized worst-case cost over broadened latent parameter ranges $\tilde{\Psi}^b(\mathbf{P}^*)$ captures this by expanding the range of possible flip angles from $\mathcal{K}_t = [0.9, 1.1]$ to $\mathcal{K}_b = [0.5, 2]$ to account for factor-of-two spatial variation in relative flip angle κ . As a result, we find that the properties of “broad” search criterion $\tilde{\Psi}^b(\cdot)$ provide a stronger reason to select the $(0, 2)$ scan for joint T_1, T_2 estimation in the brain than the properties of “tight” search criterion $\tilde{\Psi}^t(\cdot)$.

S.I.B Relation to Prior Art

To relate our work to other scan design methods, we apply min-max scan design to the well-studied problem of scan design for T_1 estimation from two SPGR scans and compare our results with those of

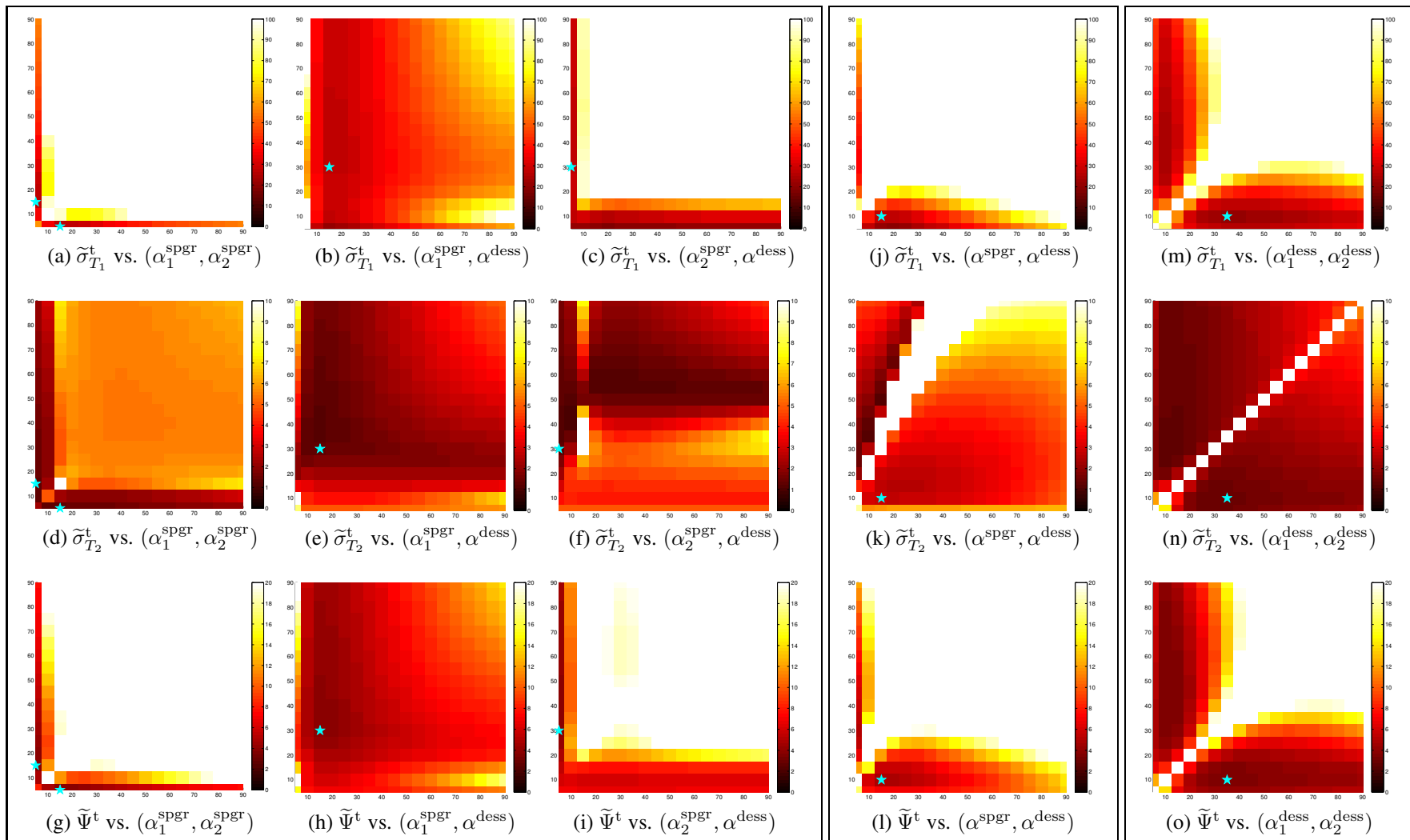


Figure S.1: Worst-case standard deviations $\tilde{\sigma}_{T_1}^t$ (top), $\tilde{\sigma}_{T_2}^t$ (middle), and cost $\tilde{\Psi}^t$ (bottom), versus pairs of nominal flip angles, holding other scan parameters fixed at selected profile \mathbf{P}^* . Subfigures (a)-(i), (j)-(l), and (m)-(o) correspond to scan profiles containing $(C_{\text{SPGR}}, C_{\text{DESS}}) = (2, 1), (1, 1),$ and $(0, 2)$ SPGR and DESS scans, respectively. Selected scan parameters (starred) are within $\delta = 1\%$ of global minimizers and retain as much estimator precision as possible over a wide range of latent object parameters. All axes range from 5 to 90 degrees, in 5-degree increments. Colorbar ranges are $[0, 100]$, $[0, 10]$, and $[0, 20]$ milliseconds for rows of $\tilde{\sigma}_{T_1}^t$, $\tilde{\sigma}_{T_2}^t$, and $\tilde{\Psi}^t$ subfigures, respectively. The optimized $(0, 2)$ profile appears most robust to flip angle variation.

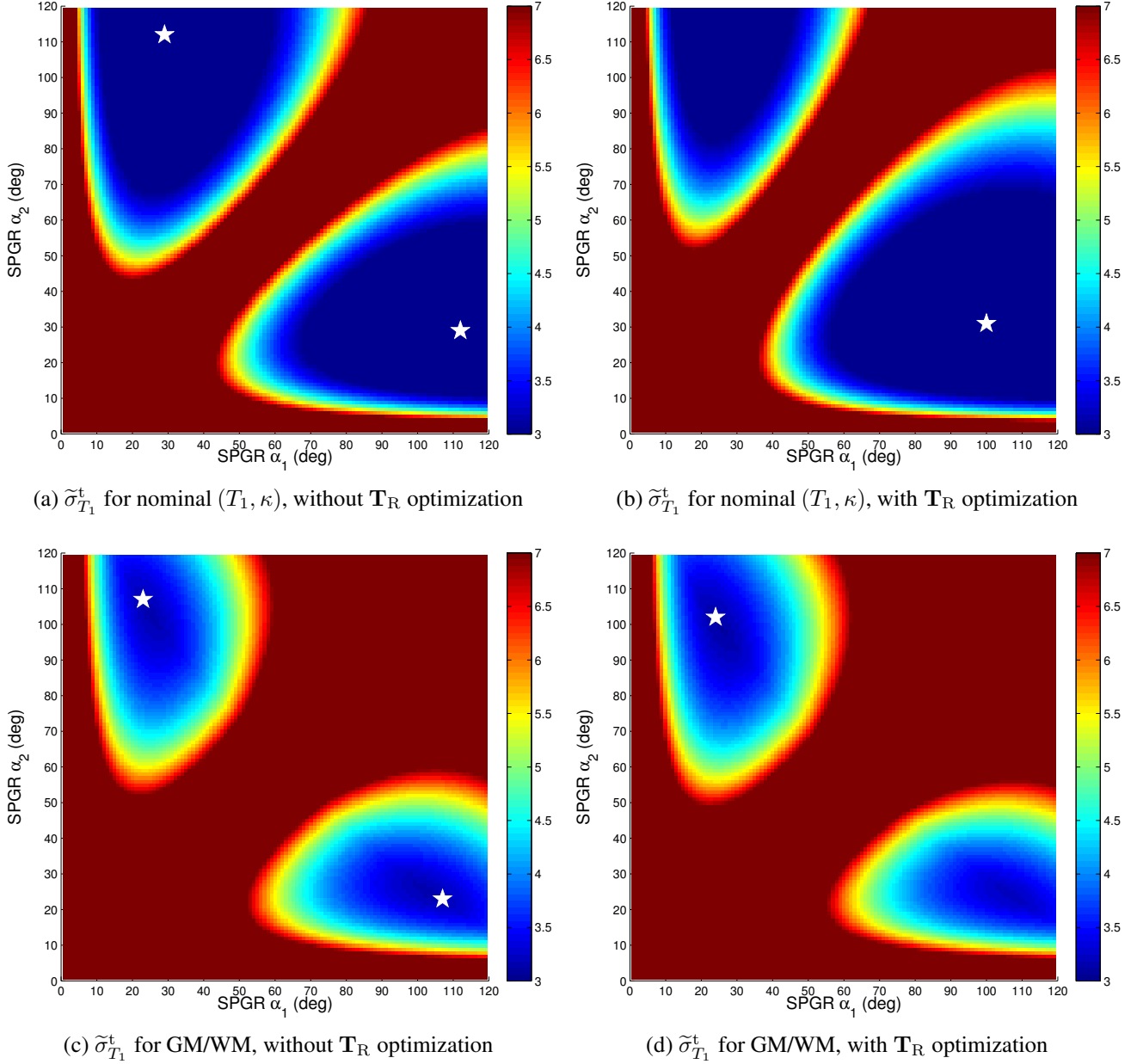


Figure S.2: Worst-case standard deviation $\tilde{\sigma}_{T_1}^t$ versus pairs of nominal SPGR flip angles, holding other scan parameters fixed at selected profile \mathbf{P}^* . Fig. S.2a (replicated from [2]) illustrates $\tilde{\sigma}_{T_1}^t$ (at single-point design ranges $\mathcal{X}_t := \mathcal{M}_{E,t} \times \mathcal{T}_{1,t} \leftarrow (1, 1000\text{ms})$ and $\mathcal{N}_t := \mathcal{K} \leftarrow 1$) as flip angles are varied but $\mathbf{T}_R \leftarrow [800, 800]^T\text{ms}$ remains fixed. Fig. S.2b (related to [3]) shows that lower $\tilde{\sigma}_{T_1}^t$ is achievable by allowing \mathbf{T}_R to vary as well. Figs. S.2c and S.2d illustrate how corresponding optimized designs change when $\tilde{\sigma}_{T_1}^t$ is instead evaluated over GM/WM ROIs $\mathcal{X}_t \leftarrow 1 \times [800, 1400]\text{ms}$ and $\mathcal{K}_t \leftarrow [0.9, 1.1]$. Selected scan parameters (starred) are within $\delta = 1\%$ of global minimizers. Colorbar ranges are in milliseconds.

[2, 3]. We study [2, 3] over other works [4–6] because our purpose here is to demonstrate the utility of considering a range of design parameters, perhaps through our min-max formulation. The methods of [2, 3] are amenable to this purpose, as they study special cases of min-max optimization problem (6) in which the object parameter space $\mathcal{X}_t \times \mathcal{N}_t$ is a single point.

Subfigure [Method]	S.2a [2]	S.2b [3]	S.2c [1]	S.2d [1]
$\mathcal{T}_{1,t}$	1000ms	1000ms	[800, 1400]ms	[800, 1400]ms
\mathcal{K}_t	1	1	[0.9, 1.1]	[0.9, 1.1]
$\mathcal{T}_{R,SPGR}$	[800, ∞)ms	[12.2, ∞)ms	[800, ∞)ms	[12.2, ∞)ms
$\mathcal{A}_{0,SPGR}$	[1, 120] $^\circ$	[1, 120] $^\circ$	[1, 120] $^\circ$	[1, 120] $^\circ$
$T_{R,max}$	1600ms	1600ms	1600ms	1600ms
$\hat{\alpha}_0^{SPGR}$	(29, 112) $^\circ$	(31, 100) $^\circ$	(23, 107) $^\circ$	(24, 102) $^\circ$
\hat{T}_R^{SPGR}	(800, 800)ms	(1010, 590)ms	(800, 800)ms	(870, 730)ms
$\tilde{\sigma}_{T_1}^t(\mathbf{P}^*)$, single-pt $\mathcal{X}_t \times \mathcal{N}_t$	1.97ms	1.89ms	2.04ms	1.99ms
$\tilde{\sigma}_{T_1}^t(\mathbf{P}^*)$, WM/GM $\mathcal{X}_t \times \mathcal{N}_t$	3.47ms	3.41ms	3.18ms	3.13ms
Run Time	6s	5m11s	2m29s	2h5m13s

Table S.1: Description and performance summary of four methods for optimization of two SPGR scans for precise T_1 estimation. Columns correspond with subfigures of Fig. S.2. Column 2 replicates results given in [2], which optimizes α at fixed \mathbf{T}_R and nominal \mathbf{x}, ν values. Column 3 uses ideas presented in [3] to improve [2] by optimizing both α and \mathbf{T}_R , under a time constraint. Columns 4-5 repeat the experiments of Columns 2-3, but over $\mathcal{X}_t \times \mathcal{N}_t$ corresponding to WM/GM at 3T.

Table S.1 summarizes how, with appropriate choices of parameter spaces, weights, and constraints, previous methods relate to min-max scan design (corresponding illustrations provided in Fig. S.2). To assess the utility of min-max design, we compare worst-case standard deviation $\tilde{\sigma}_{T_1}^t$ (computed with unity M_0 and constant noise variance $\sigma^2 \leftarrow 1.49 \times 10^{-7}$ as in the Manuscript) over the same WM/GM parameter space $\mathcal{X}_t \times \mathcal{N}_t$. Comparing Columns 2 and 4, we observe an 8.7% reduction in WM/GM $\tilde{\sigma}_{T_1}^t$ through min-max consideration for flip angle optimization. Similarly comparing columns 3 and 5, we observe an 8.6% reduction in WM/GM $\tilde{\sigma}_{T_1}^t$ through min-max consideration for flip angle and repetition time optimization. Each min-max grid-search takes roughly $25\times$ longer than its min-only counterpart. This substantial increase in (offline) computation time could likely be reduced through gradient-based optimization, at the expense of forgoing global for instead local optima.

S.II Latent Object Parameter Estimation from Optimized Scan Profiles

To experimentally validate scan designs, we require a method to obtain parameter estimates from data collected using the optimized scan parameters \mathbf{P}^* . Here, we describe maximum-likelihood (ML) and regularized least-squares (RLS) optimization approaches for latent object parameter estimation.

When the reconstructed images have V voxels centered at positions $\mathbf{r}_1, \dots, \mathbf{r}_V$, an ML estimator $\hat{\mathbf{X}}_{ML}(\mathbf{N}, \mathbf{P}^*)$ minimizes over \mathbf{X} the negative log-likelihood

$$\Psi^{ML}(\mathbf{X}; \mathbf{N}, \mathbf{P}^*) = \frac{1}{2} \left\| \Sigma^{-1/2} (\mathbf{Y} - \mathbf{F}(\mathbf{X}; \mathbf{N}, \mathbf{P}^*)) \right\|_F^2, \quad (\text{S.1})$$

where matrices $\mathbf{Y} := [\mathbf{y}(\mathbf{r}_1), \dots, \mathbf{y}(\mathbf{r}_V)] \in \mathbb{C}^{D \times V}$, $\mathbf{X} := [\mathbf{x}(\mathbf{r}_1), \dots, \mathbf{x}(\mathbf{r}_V)] \in \mathbb{C}^{L \times V}$, and $\mathbf{N} := [\nu(\mathbf{r}_1), \dots, \nu(\mathbf{r}_V)] \in \mathbb{C}^{K \times V}$ are discretizations over V voxel locations of vector counterparts; matrix function $\mathbf{F} : \mathbb{C}^{L \times V} \times \mathbb{C}^{K \times V} \times \mathbb{C}^{P \times D} \mapsto \mathbb{C}^{D \times V}$ naturally extends \mathbf{f} ; \mathbf{P}^* remains the optimized scan profile from (9); and $\|\cdot\|_F$ denotes the Frobenius norm.

Often, it is reasonable to assume that each latent object parameter map is (possibly piecewise) smooth. To exploit this prior knowledge, we estimate \mathbf{X} by minimizing over search space \mathcal{X}^V an extension of (S.1) that includes regularization:

$$\widehat{\mathbf{X}}_{\text{RLS}}(\mathbf{N}, \mathbf{P}^*) \in \arg \min_{\mathbf{X} \in \mathcal{X}^V} \Psi^{\text{RLS}}(\mathbf{X}; \mathbf{N}, \mathbf{P}^*), \quad \text{where} \quad (\text{S.2})$$

$$\Psi^{\text{RLS}}(\mathbf{X}; \mathbf{N}, \mathbf{P}^*) = \Psi^{\text{ML}}(\mathbf{X}; \mathbf{N}, \mathbf{P}^*) + \sum_{l=1}^L R_l([\mathbf{X}]_l^T) \quad (\text{S.3})$$

and $[\cdot]_r$ extracts the r th row of its argument. Here, we have introduced regularizer functions $R_l(\cdot) : \mathbb{C}^V \mapsto \mathbb{R}$ for $l \in \{1, \dots, L\}$, which in this work are chosen as

$$R_l(\cdot) := \beta_l \sum_{j=1}^J \phi_l([\mathbf{C}(\cdot)]_j), \quad (\text{S.4})$$

where β_l is a regularization parameter; $\phi_l : \mathbb{C} \mapsto \mathbb{R}$ is a (possibly edge-preserving) convex penalty function, selected based on expected properties of the l th latent object parameter; $\mathbf{C} \in \mathbb{R}^{J \times V}$ is a finite differencing matrix; and j indexes a total J direction-dependent differencing operations.

Typically, $\Psi^{\text{RLS}}(\mathbf{X}; \mathbf{N}, \mathbf{P}^*)$ is non-convex in \mathbf{X} , precluding global optimization. We instead seek a local minimizer of (S.3) using the projected Levenberg-Marquardt method [7] with a step-halving line search to ensure monotonic convergence in cost.

For non-convex cost functions like (S.3), initialization quality is important. In this work, we initialize (S.2) by first isolating nonlinear dependencies via the “variable-projection” method [8], and then minimizing (S.1) using a nonlinear least-squares (NLS) algorithm. Specifically, we note that $\Psi^{\text{ML}}(\mathbf{X}; \mathbf{N}, \mathbf{P}^*)$ is voxel-wise separable, and thereby find a global minimizer of (S.1) in a single iteration of matching pursuit [9, 10] with a precomputed dictionary of signal vectors.

Following an analysis similar to that of [11] for the NLS objective (S.1), one can show that if \mathbf{f} is a smooth, injective mapping and dictionary quantization error is neglected, then $\widehat{\mathbf{X}}_{\text{ML}}(\mathbf{N}, \mathbf{P}^*)$ is asymptotically efficient. At reasonable noise levels, we thus expect \mathbf{P}^* to permit low ML estimation variance. For suitable regularizers, minimizing (S.3) with initialization $\widehat{\mathbf{X}}_{\text{ML}}(\mathbf{N}, \mathbf{P}^*)$ then only further reduces variance.

Even for nonlinear $\mathbf{f}(\cdot)$, the ML estimate $\widehat{\mathbf{X}}_{\text{ML}}$ is asymptotically unbiased. For Gaussian noise models, increasing sample size is statistically equivalent to increasing signal-to-noise ratio (SNR). Thus, in regions where the data provides sufficiently high SNR (and is thus approximately Gaussian-distributed even in magnitude [12]), $\widehat{\mathbf{X}}_{\text{ML}}$ will exhibit negligible bias, and the CRB can be used to reliably predict ML estimation error. Table II in Section IV empirically explores the validity of this high-SNR assumption, through simulations at realistic noise levels.

S.III Numerical Simulations

Fig. S.3 displays latent object parameter estimates $\widehat{\mathbf{T}}_1^{\text{ML}}$ and $\widehat{\mathbf{T}}_2^{\text{ML}}$ from the optimized scan profiles alongside ($5 \times$ magnified) absolute differences with respect to the ground truth (corresponding sample statistics within WM/GM regions of interest are summarized in Table II). Difference images suggest that, with careful scan optimization, all three scan profiles permit \mathbf{T}_1 and \mathbf{T}_2 to be jointly estimated with low error.

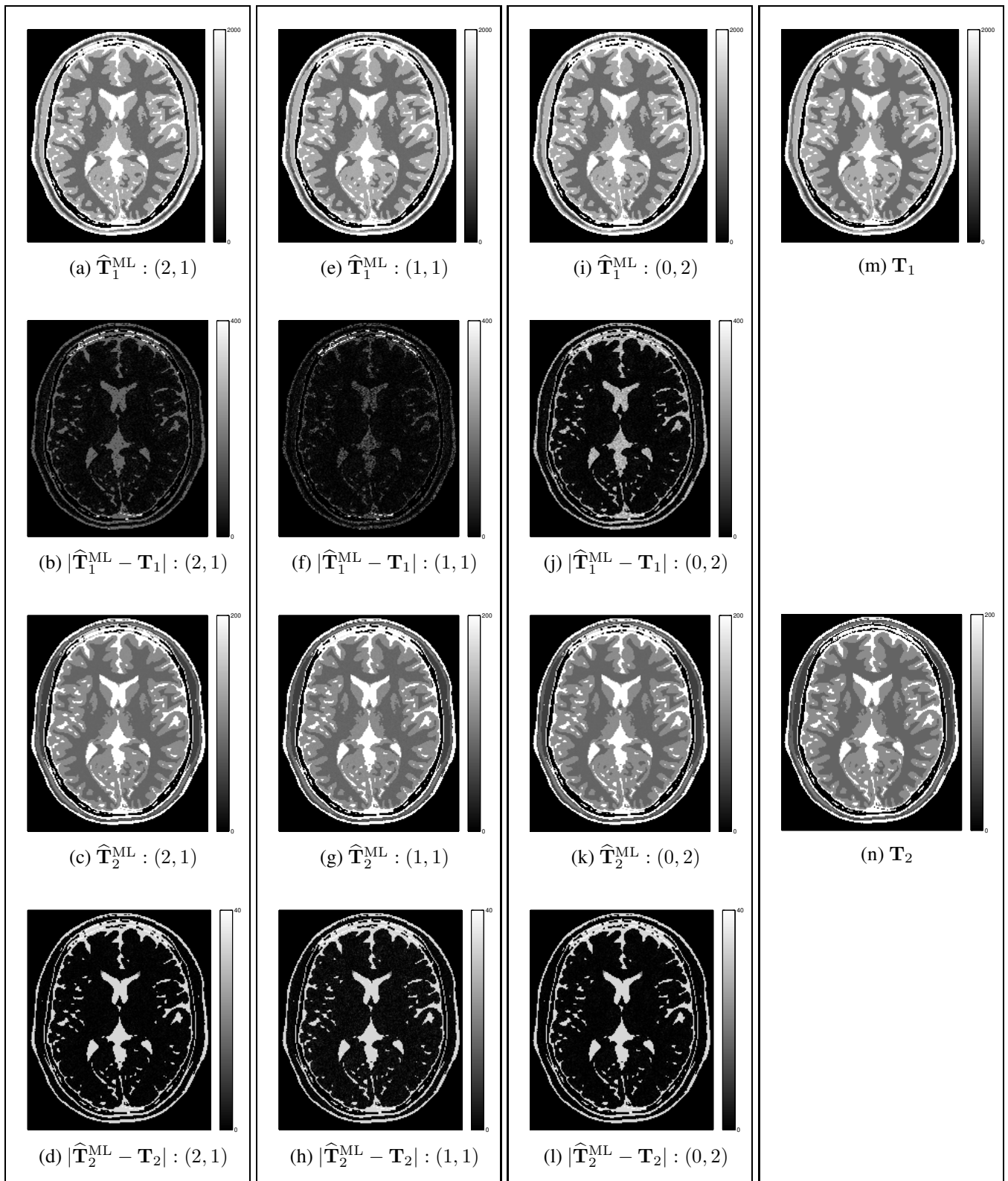
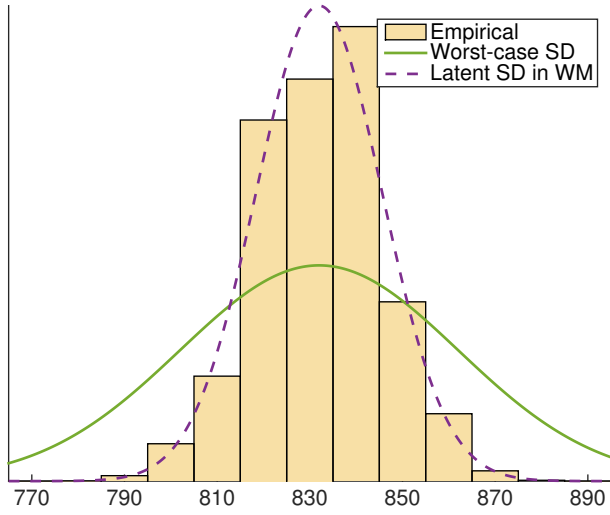
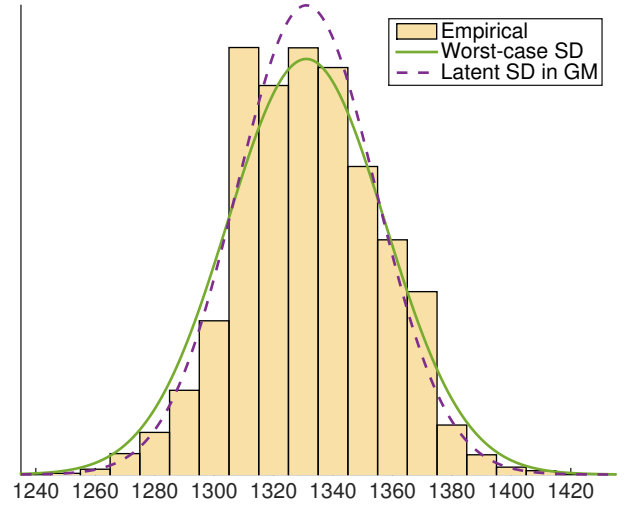


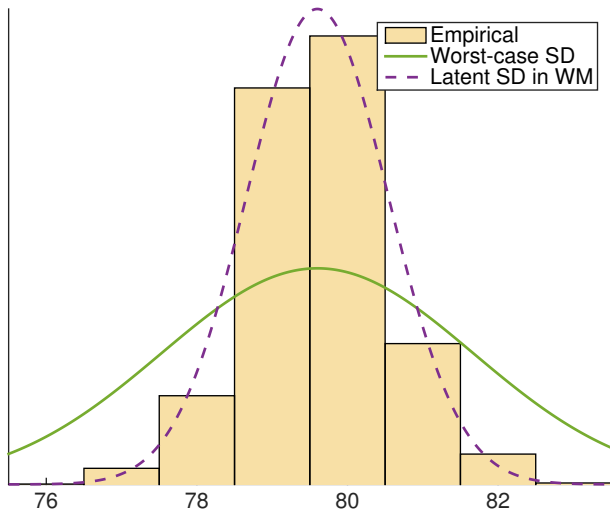
Figure S.3: T_1 and T_2 ML estimates and corresponding errors, from data synthesized using the optimized scan profiles in Table I. Subfigures (a)-(d), (e)-(h), and (i)-(l) correspond to scan profiles $(C_{\text{SPGR}}, C_{\text{DESS}}) = (2, 1), (1, 1),$ and $(0, 2)$ SPGR and DESS scans, respectively. Colorbar ranges corresponding to T_1^{ML} and T_2^{ML} estimates are $[0, 2000]$ ms and $[0, 200]$ ms, respectively. Magnitude error maps are computed with respect to latent, ground truth (m) T_1 and (n) T_2 maps, and are respectively presented with $5\times$ magnified colorbar ranges $[0, 400]$ ms and $[0, 40]$ ms to aid comparison.



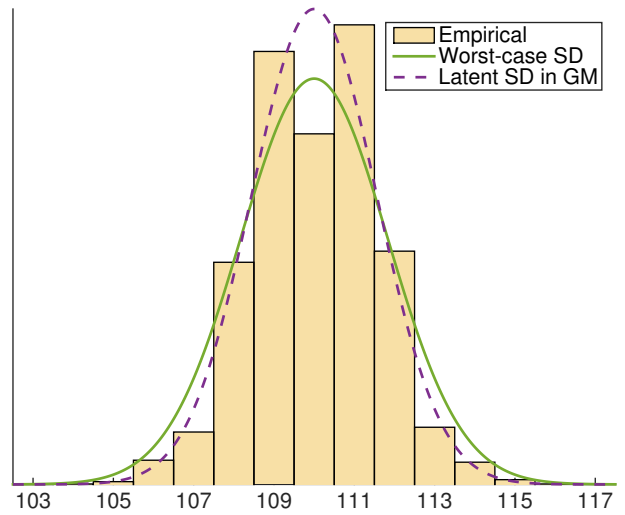
(a) \hat{T}_1^{ML} (ms) in voxels with true WM-like $T_1 \leftarrow 832$



(b) \hat{T}_1^{ML} (ms) in voxels with true GM-like $T_1 \leftarrow 1331$



(c) \hat{T}_2^{ML} (ms) in voxels with true WM-like $T_2 \leftarrow 79.6$



(d) \hat{T}_2^{ML} (ms) in voxels with true GM-like $T_2 \leftarrow 110$

Figure S.4: Histograms of T_1 and T_2 estimates from noisy independent measurements of a *single* nominal WM or GM value. In each plot, two normal distributions are overlaid, each with latent means T_1 and T_2 . In (a)-(b) and (c)-(d), the solid green curve is $\mathcal{N}(T_1, (\tilde{\sigma}_{T_1}^t)^2)$ and $\mathcal{N}(T_2, (\tilde{\sigma}_{T_2}^t)^2)$, respectively. In (a)-(d), the dashed maroon curves have variances computed from the Fisher information at *a priori* unknown T_1, T_2 values in WM or GM. These plots correspond to an optimized (0, 2) scan profile; analogous plots for other profiles are visually similar. At realistic noise levels, parameter estimates distribute with minimal bias and near-Gaussian shape. Thus, the CRB can be used to reliably approximate \hat{T}_1^{ML} and \hat{T}_2^{ML} errors.

Fig. S.4 histograms (voxel-wise independent) ML estimates \hat{T}_1^{ML} and \hat{T}_2^{ML} from the (0, 2) scan profile. Each histogram is over a WM or GM ROI, within which all voxels are assigned the same single-component true T_1 and T_2 nominal value, listed in Table II.

Overlaid in dashed maroon are normal distributions with latent means T_1 and T_2 and variances computed from the Fisher matrix at T_1, T_2 values in WM or GM. It is apparent that despite finite SNR and Rician noise, \hat{T}_1^{ML} and \hat{T}_2^{ML} exhibit negligible bias and near-Gaussian shape, suggesting locally linear behavior of the DESS signal model in T_1 and T_2 (\hat{T}_1^{ML} and \hat{T}_2^{ML} distributions from other profiles are similar).

The subfigures of Fig. S.4 superimpose in solid green a second set of normal distributions, with the same means T_1 and T_2 as before, but worst-case standard deviations $\tilde{\sigma}_{T_1}^t$ and $\tilde{\sigma}_{T_2}^t$. The separations between these distribution pairs visually depict how estimator variances specific to WM or GM T_1 and T_2 values differ from worst-case variances. Using the fixed latent object parameters to optimize scan profiles can tailor scans for precise estimation in *either* WM *or* GM. In contrast, the proposed min-max formulation finds scan parameters that ensure precise estimation in *both* WM *and* GM.

S.IV Flip Angle Scaling Calibration

In initial experiments, we found that even small (*e.g.*, $\sim 5\%$) modifications of flip angle scaling estimate $\hat{\kappa}$ from Bloch-Siegert (BS) shifted SPGR scans resulted in significant (*e.g.*, $\sim 10\text{-}15\%$) changes in SPGR/DESS \hat{T}_1 estimates. Here, we investigate possible $\hat{\kappa}$ estimation bias by comparing (via a separate study) $\hat{\kappa}$ from Bloch-Siegert (BS) [13] versus reference Double Angle (DA) [14] measurements.

We collect 8-channel BS and DA data in a structureless FIRST-BIRN gel phantom [15] ($T_1 \approx 520\text{ms}$ via separate IR measurements). For DA (SPGR) scans, we prescribe nominal flip angles $\hat{\alpha}_0 \leftarrow [45^\circ, 90^\circ]^\top$ and long repetition times $\mathbf{T}_R \leftarrow [3200, 3200]^\top\text{ms}$. Except for a reduced $256 \times 256 \times 6$ matrix, all other BS and SPGR acquisition details are the same as in Section IV.B.1.

We separately normalize and combine (via an extension of [16]) each pair of BS and DA coil datasets. To reduce errors due to \mathbf{k} -space truncation in regularized κ estimates, we mask out coil-combined image voxels outside and very near the phantom encasing. Initializing with respective method-of-moments estimates, we apply the methods of [17] and [18] to produce regularized κ estimates from coil-combined BS versus DA images.

Fig. S.5 reveals that well inside the phantom, BS and DA κ estimates exhibit paraboloidal spatial profiles (as expected), but differ in scaling. Specifically, within a centered ROI of 6758 voxels, the ratio of RLS DA $\hat{\kappa}$ to RLS BS $\hat{\kappa}$ has ROI sample mean \pm ROI sample standard deviation of 1.050 ± 0.0044 .

To reduce error propagation due to $\hat{\kappa}$ bias but retain the speed of BS acquisitions, we choose to scale up BS κ estimates in all phantom and *in vivo* experiments by 5.0%. We find empirically that even this crude correction factor greatly improves \hat{T}_1 agreement across SPGR/DESS and reference IR/SE scan profiles.

S.V Experimental Details

This section provides further details on phantom and *in vivo* experiments discussed in Sections IV.B and IV.C. Sections S.V.A and S.V.B provide phantom reconstruction details about SPGR/DESS and IR/SE

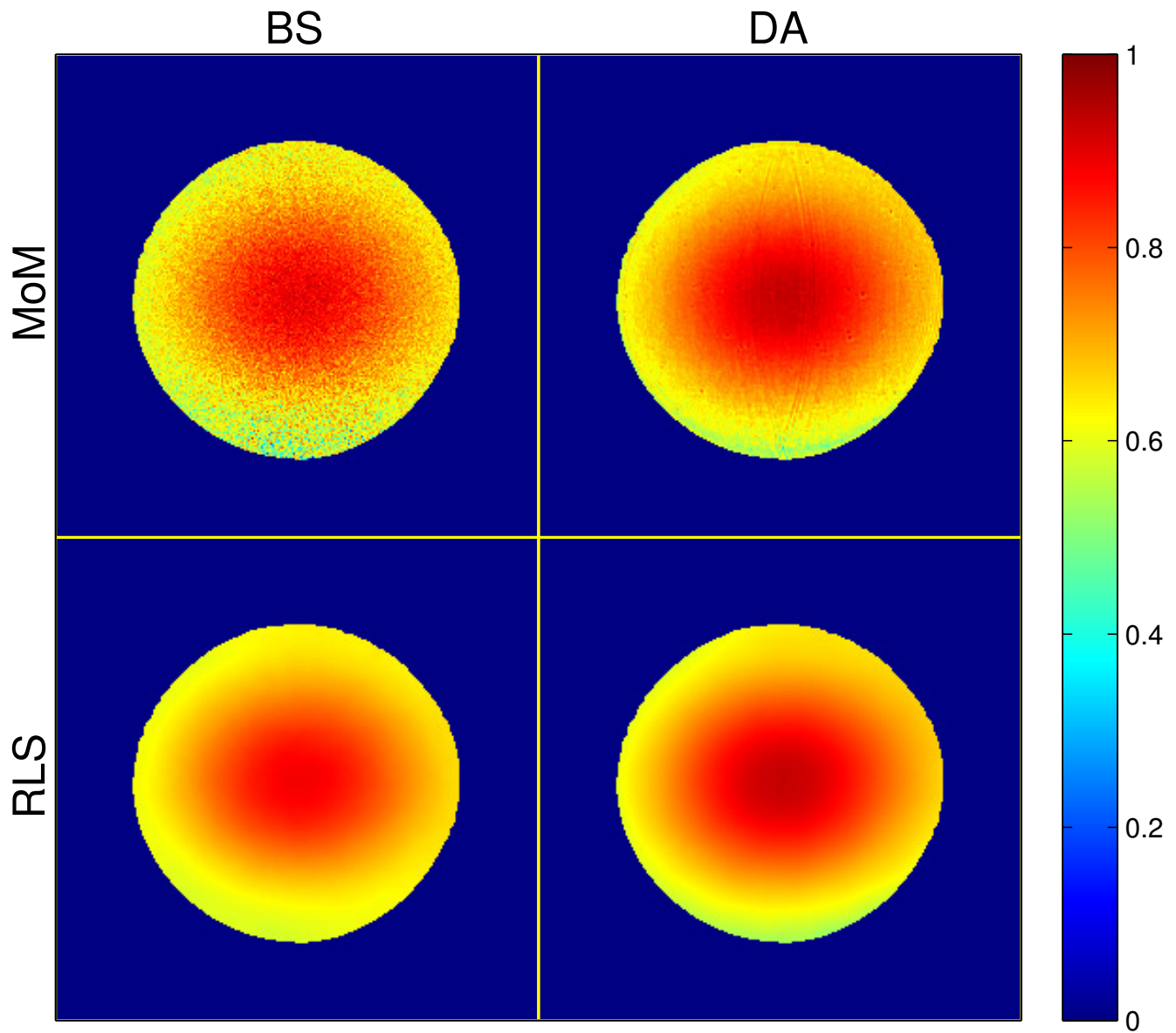


Figure S.5: Method of Moments (top) and RLS (bottom) estimates of flip angle scaling κ in a FIRST-BIRN gel phantom, from Bloch-Siegert (left) and Double-Angle (right) data. Well away from the phantom encasing, both estimates exhibit a paraboloidal spatial profile, but differ in scaling by $4.8 \pm 0.71\%$.

experiments. Unless explicitly mentioned in Section IV.C, these details pertain to brain reconstructions as well. Sections S.V.C and S.V.D discuss additional phantom and *in vivo* images and tables; in addition, Section S.V.D provides image registration details.

S.V.A SPGR/DESS (Phantom) Reconstructions

We acquire all phantom datasets using a GE Discovery™ MR750 3.0T scanner with an 8-channel receive head array. We separately normalize and combine coil data from each scan profile using a natural extension of [16] to the case of multiple datasets. For each optimized SPGR/DESS scan profile \mathbf{P}^* , we pre-cluster known parameter maps \mathbf{N} into 10 clusters using *k*-means++ [19] and use each of the 10 cluster means to compute a corresponding dictionary of signal vectors from 300 T_1 and T_2 values logarithmically spaced between $[10^{1.5}, 10^{3.5}]$ and $[10^{0.5}, 10^3]$, respectively. We then iterate over clusters and use each dictionary in conjunction with corresponding coil-combined magnitude image data to produce ML parameter estimates $\hat{\mathbf{X}}_{\text{ML}}(\mathbf{N}, \mathbf{P}^*)$. We subsequently solve RLS problem (S.2) with initialization $\hat{\mathbf{X}}_{\text{ML}}(\mathbf{N}, \mathbf{P}^*)$ to obtain regularized estimates $\hat{\mathbf{X}}_{\text{RLS}}(\mathbf{N}, \mathbf{P}^*)$ for each \mathbf{P}^* . We design regularizers to encourage parameter estimates from different scan profiles to exhibit similar levels of smoothness. Letting $l \in \{1, 2, 3\}$ enumerate latent object parameters $\{\mathbf{M}_{0/E}, \mathbf{T}_1, \mathbf{T}_2\}$, we choose mild regularization parameters $(\beta_1, \beta_2, \beta_3) := D \times (2^{-26}, 2^{-21}, 2^{-23})$ to scale with the number of datasets. For all scan profiles, we use a corner-rounded approximation to the ℓ_1 potential function,

$$\phi_l(\cdot) := \gamma_l^2 \left[\sqrt{1 + |\cdot/\gamma_l|^2} - 1 \right] \quad (\text{S.5})$$

where $(\gamma_1, \gamma_2, \gamma_3) := (2^{-2}, 2^5 \text{ ms}, 2^2 \text{ ms})$ are fixed to values on the order of anticipated standard deviations. We iteratively update \mathbf{X} until convergence criterion

$$\|\mathbf{X}^{(n)} - \mathbf{X}^{(n-1)}\|_F < 10^{-7} \|\mathbf{X}^{(n)}\|_F \quad (\text{S.6})$$

is satisfied. For all steady-state profiles tested, ML initializations and RLS reconstructions of phantom datasets require less than 3m30s and 9s, respectively.

S.V.B IR/SE (Phantom) Reconstructions

We first jointly coil-combine all 8-channel IR and SE phantom datasets to produce complex images. We next estimate \mathbf{T}_1 along with nuisance parameters $\mathbf{M}_0 \exp(-T_E/T_2)$ and inversion efficiency map ϵ via (S.1) and (S.3) from the 4 complex coil-combined IR images. By using the same flip angle scaling map $\hat{\kappa}$ as is used for SPGR/DESS profiles, we estimate \mathbf{T}_1 using a signal model similar to one proposed in [20], which accounts for imperfect excitation/refocusing and imperfect inversion. We then take both \mathbf{T}_1 and κ as known and estimate \mathbf{T}_2 along with nuisance parameter \mathbf{M}_0 (accounting for imperfect excitation/refocusing and incomplete recovery) via (S.1) and (S.3) from the 4 complex coil-combined SE images. We hold all other reconstruction details identical to those of SPGR/DESS reconstructions. For all steady-state scan profiles tested, ML initializations and RLS reconstructions of brain datasets require less than 3m and 7s, respectively.

As an aside: we initially attempted to circumvent sequential \mathbf{T}_1 , then \mathbf{T}_2 estimation by instead jointly estimating \mathbf{M}_0 , \mathbf{T}_1 , \mathbf{T}_2 , and ϵ from the IR and SE datasets together. Even using magnitude data and signal models, this resulted in heavily biased parameter maps, possibly due to the dependence of adiabatic inversion efficiency on relaxation parameters [21].

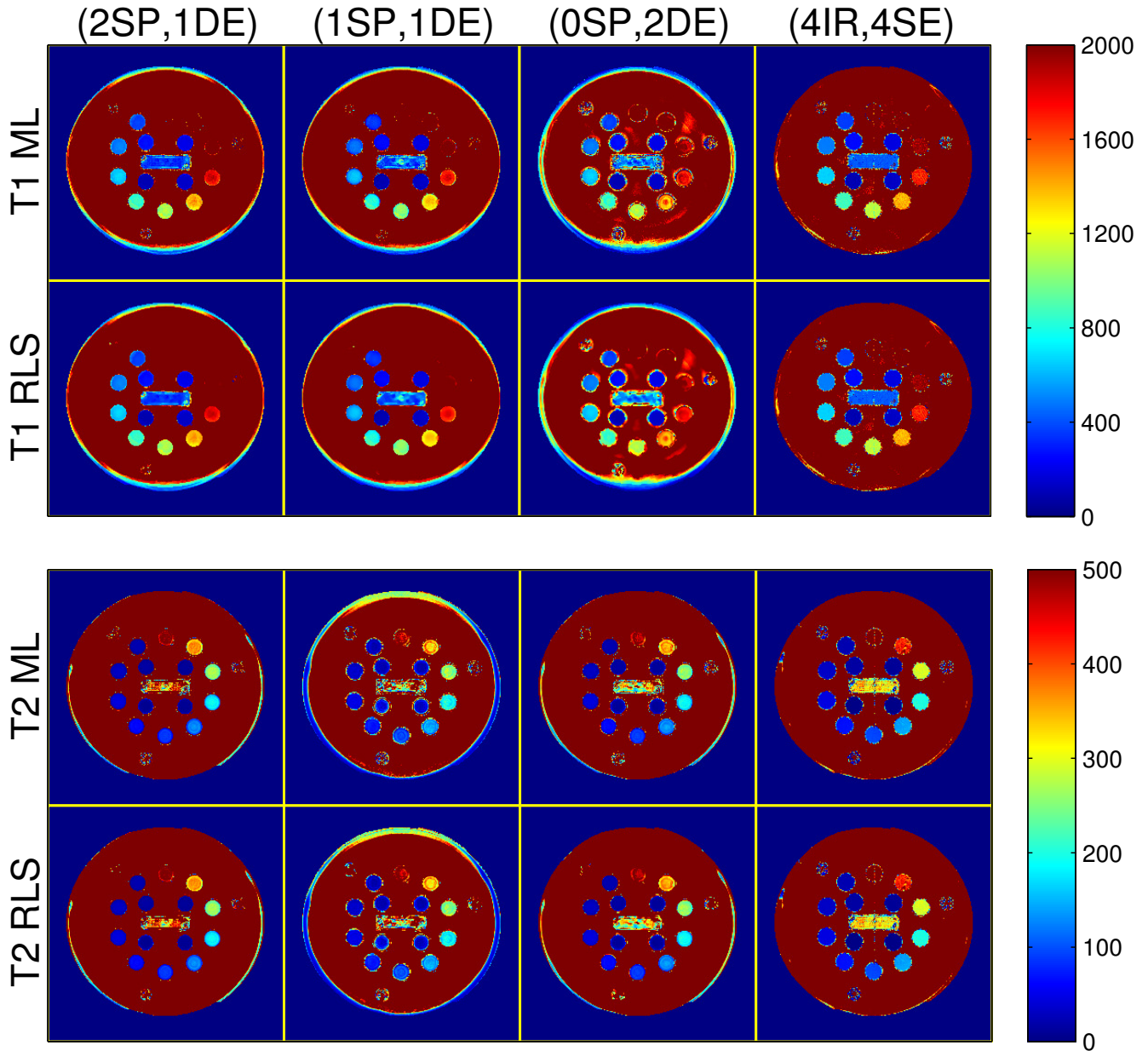


Figure S.6: Colorized T_1 and T_2 ML and RLS estimates from an HPD[®] quantitative phantom. Columns correspond to scan profiles consisting of (2 SPGR, 1 DESS), (1 SPGR, 1 DESS), (0 SPGR, 2 DESS), and (4 IR, 4 SE) acquisitions. Rows distinguish T_1 and T_2 ML and RLS estimators. Fig. S.7 provides identical grayscale images which enumerate vials. Colorbar ranges are in milliseconds.

S.V.C Phantom Images and Tables

Figs. S.6 and S.7 compare phantom T_1 and T_2 ML and RLS estimates in color and grayscale from optimized scan profiles. Vials are enumerated in Fig. S.7 in descending T_1 and T_2 order. Vials corresponding to tight \mathcal{X}_t and broad \mathcal{X}_b parameter ranges are highlighted with orange and yellow labels, respectively. Within these vials of interest, parameter maps from different scans appear visually similar.

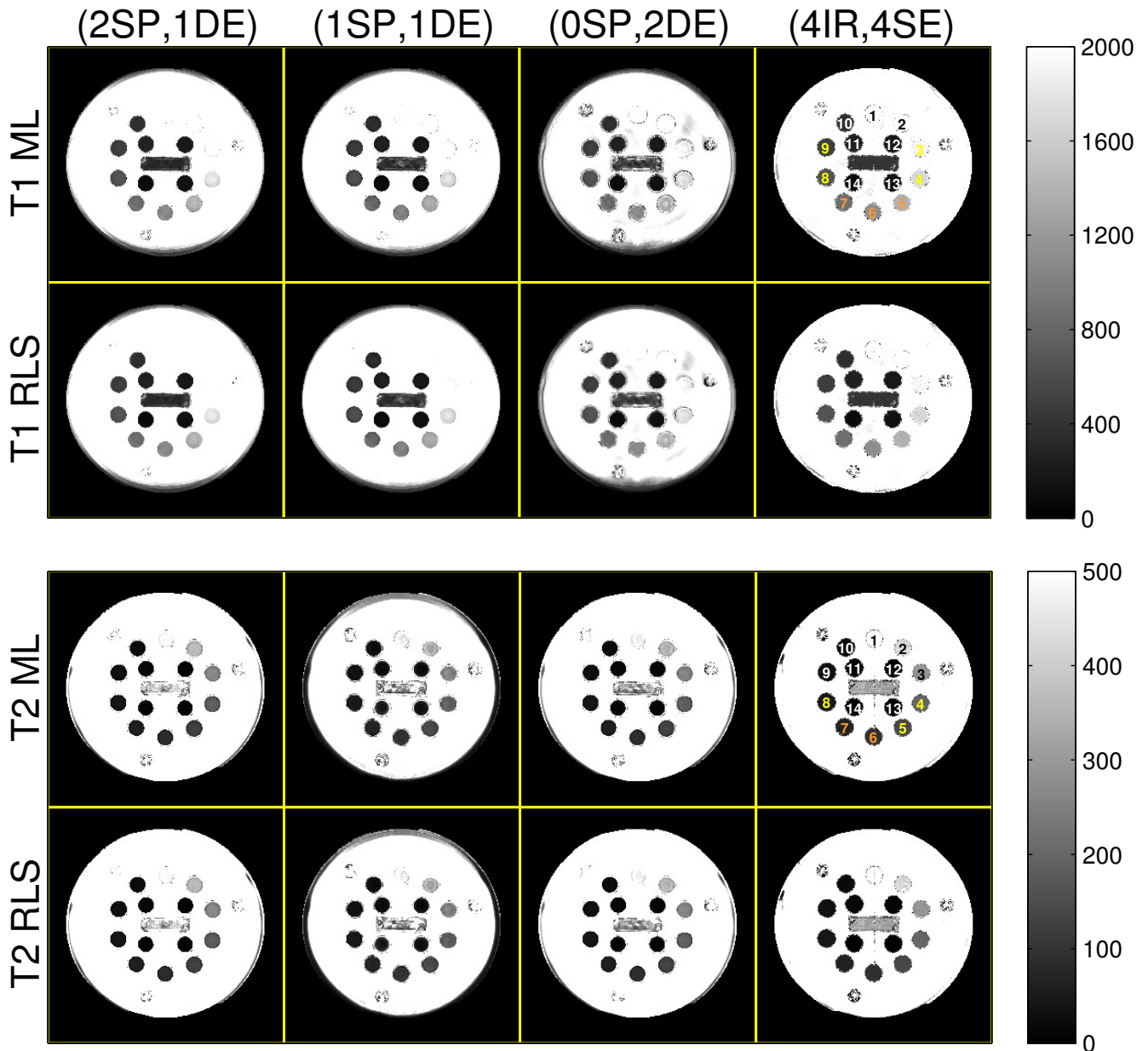


Figure S.7: Grayscale T_1 and T_2 ML and RLS estimates from an HPD[®] quantitative phantom. Columns correspond to scan profiles consisting of (2 SPGR, 1 DESS), (1 SPGR, 1 DESS), (0 SPGR, 2 DESS), and (4 IR, 4 SE) acquisitions. Rows distinguish T_1 and T_2 ML and RLS estimators. Vials are enumerated and color-coded to correspond with data points in Fig. S.8. Fig. S.6 provides identical colorized images. Colorbar ranges are in milliseconds.

In higher- T_1 vials (and the surrounding water), more bias is apparent in \hat{T}_1 ML and RLS estimates from the (0, 2) scan profile than from the (2, 1) and (1, 1) scan profiles. With the signal models used in this study, the images suggest that scan profiles consisting of at least one SPGR scan may offer increased protection against T_1 estimation bias.

Fig. S.8 expands Fig. 1 by plotting phantom within-ROI sample statistics of both ML and RLS T_1 , T_2 estimates. Table S.2 replicates sample statistics in Fig. S.8 for vials 5-8. Compared to ML initializations,

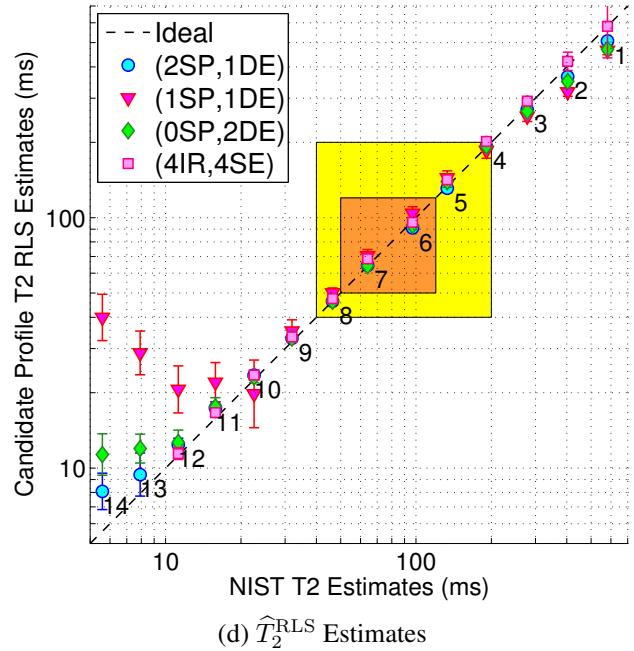
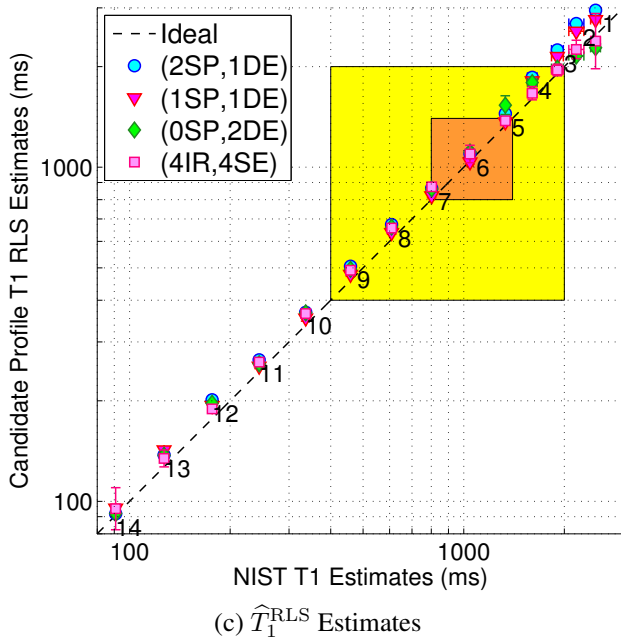
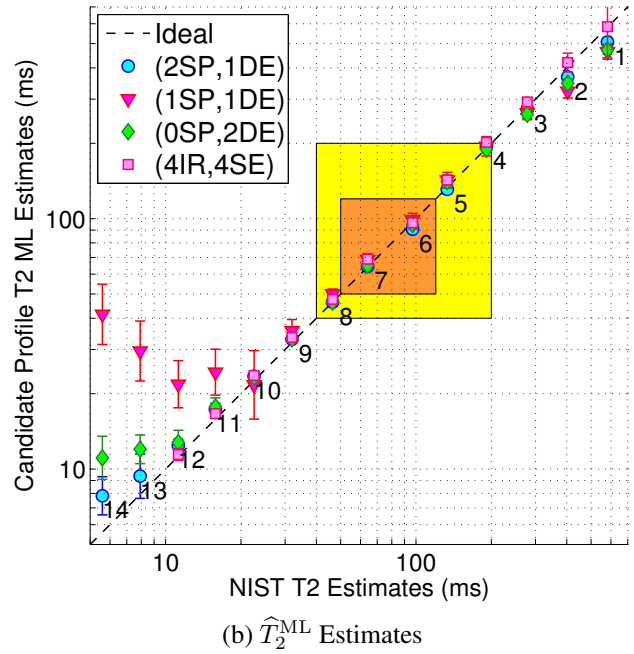
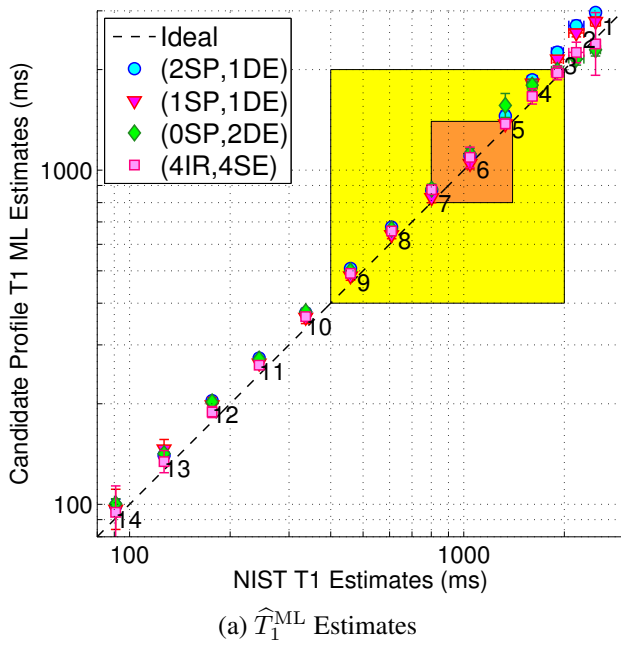


Figure S.8: Phantom within-ROI sample statistics of T_1 and T_2 estimates from optimized SPGR/DESS and reference IR/SE scan profiles, vs. NIST NMR measurements [22]. Markers and error bars indicate ROI sample means and ROI sample standard deviations within the 14 labeled and color-coded vials in Fig. S.7. Figs. S.8a-S.8b correspond with ML estimates and replicate Figs. 1a-1b for sake of comparison. Figs. S.8c-S.8d correspond with RLS estimates. Tight \mathcal{X}_t and broad \mathcal{X}_b latent parameter ranges are highlighted in orange and yellow, respectively. Table S.2 replicates sample statistics within Vials 5-8. Our MR measurements are at 293K, while NIST NMR measurements are at 293.00K. Within the designed parameter ranges, estimates from different acquisitions are in reasonable agreement with NIST measurements.

	(2SP,1DE)	(1SP,1DE)	(OSP,2DE)	(4IR,4SE)	NIST NMR
V5 $\widehat{T}_1^{\text{ML}}$	1450 ± 50.	1380 ± 41	1600 ± 130	1380 ± 44	1332 ± 0.8
V5 $\widehat{T}_1^{\text{RLS}}$	1450 ± 26	1370 ± 16	1540 ± 98	1380 ± 37	
V6 $\widehat{T}_1^{\text{ML}}$	1100 ± 30.	1050 ± 39	1120 ± 39	1100 ± 74	1044 ± 3.2
V6 $\widehat{T}_1^{\text{RLS}}$	1100 ± 15	1040 ± 14	1110 ± 16	1100 ± 64	
V7 $\widehat{T}_1^{\text{ML}}$	870 ± 22	830 ± 29	880 ± 29	870 ± 25	801.7 ± 1.70
V7 $\widehat{T}_1^{\text{RLS}}$	865 ± 7.1	820 ± 11	860 ± 18	870 ± 21	
V8 $\widehat{T}_1^{\text{ML}}$	680 ± 12	640 ± 18	670 ± 12	658 ± 8.8	608.6 ± 1.03
V8 $\widehat{T}_1^{\text{RLS}}$	674 ± 7.6	637 ± 7.4	662 ± 6.6	658 ± 7.1	
V5 $\widehat{T}_2^{\text{ML}}$	131 ± 5.5	140 ± 10.	141 ± 8.4	143 ± 4.9	133.27 ± 0.073
V5 $\widehat{T}_2^{\text{RLS}}$	131 ± 5.2	145 ± 9.1	139 ± 7.1	142 ± 4.8	
V6 $\widehat{T}_2^{\text{ML}}$	91 ± 3.5	99 ± 6.0	95 ± 4.2	96 ± 2.7	96.89 ± 0.049
V6 $\widehat{T}_2^{\text{RLS}}$	91 ± 3.4	104 ± 6.2	93 ± 3.7	96 ± 2.6	
V7 $\widehat{T}_2^{\text{ML}}$	64 ± 2.2	69 ± 3.9	65 ± 2.1	69 ± 1.2	64.07 ± 0.034
V7 $\widehat{T}_2^{\text{RLS}}$	65 ± 2.1	71 ± 4.3	64 ± 1.9	69 ± 1.2	
V8 $\widehat{T}_2^{\text{ML}}$	46 ± 1.5	50. ± 2.3	46 ± 1.1	47.6 ± 0.87	46.42 ± 0.014
V8 $\widehat{T}_2^{\text{RLS}}$	46 ± 1.5	50. ± 2.3	46 ± 1.0	47.5 ± 0.85	

Table S.2: Phantom within-ROI sample means \pm sample standard deviations of \mathbf{T}_1 and \mathbf{T}_2 estimates from optimized SPGR/DESS and reference IR/SE scan profiles, vs. NIST NMR measurements (*cf.* slide 22 of e-poster corresponding to [22]). For sake of brevity, sample statistics corresponding only to phantom vials within (or nearly within) tight design range \mathcal{X}_t (color-coded orange in Fig. S.7) are reported. Fig. S.8 plots sample statistics for all vials. ‘V#’ abbreviates vial numbers. All values are reported in milliseconds.

(weakly) regularized estimates reduce error bars without introducing substantial additional bias.

S.V.D Brain Registration Details, Images, and Tables

For each coil-combined dataset, we compute a separate 2D rigid transformation (with respect to the $T_1 = 50\text{ms}$ IR dataset) via the MATLAB[®] function `imregtform` and then apply the transformation via `imwarp`. We choose to use rigid transformations instead of affine distortions to avoid scaling; however in doing so we sacrifice compensating for small through-plane rotations. We do not find registration to substantially change subsequently estimated relaxation maps; however, this extra step substantially improves alignment of (especially cortical GM) ROIs in \widehat{T}_1 and \widehat{T}_2 estimates from different scan profiles.

Fig. S.9 expands Fig. 2 by comparing both ML and RLS \mathbf{T}_1 , \mathbf{T}_2 estimates across scan profiles. Fig. S.10 replicates Fig. S.9 in grayscale. Table S.3 is similar to Table IV, except for RLS estimates. Compared to ML counterparts, RLS estimates in general reduce within-ROI sample variation without incurring significant additional bias.

S.VI Multi-exponential Relaxation

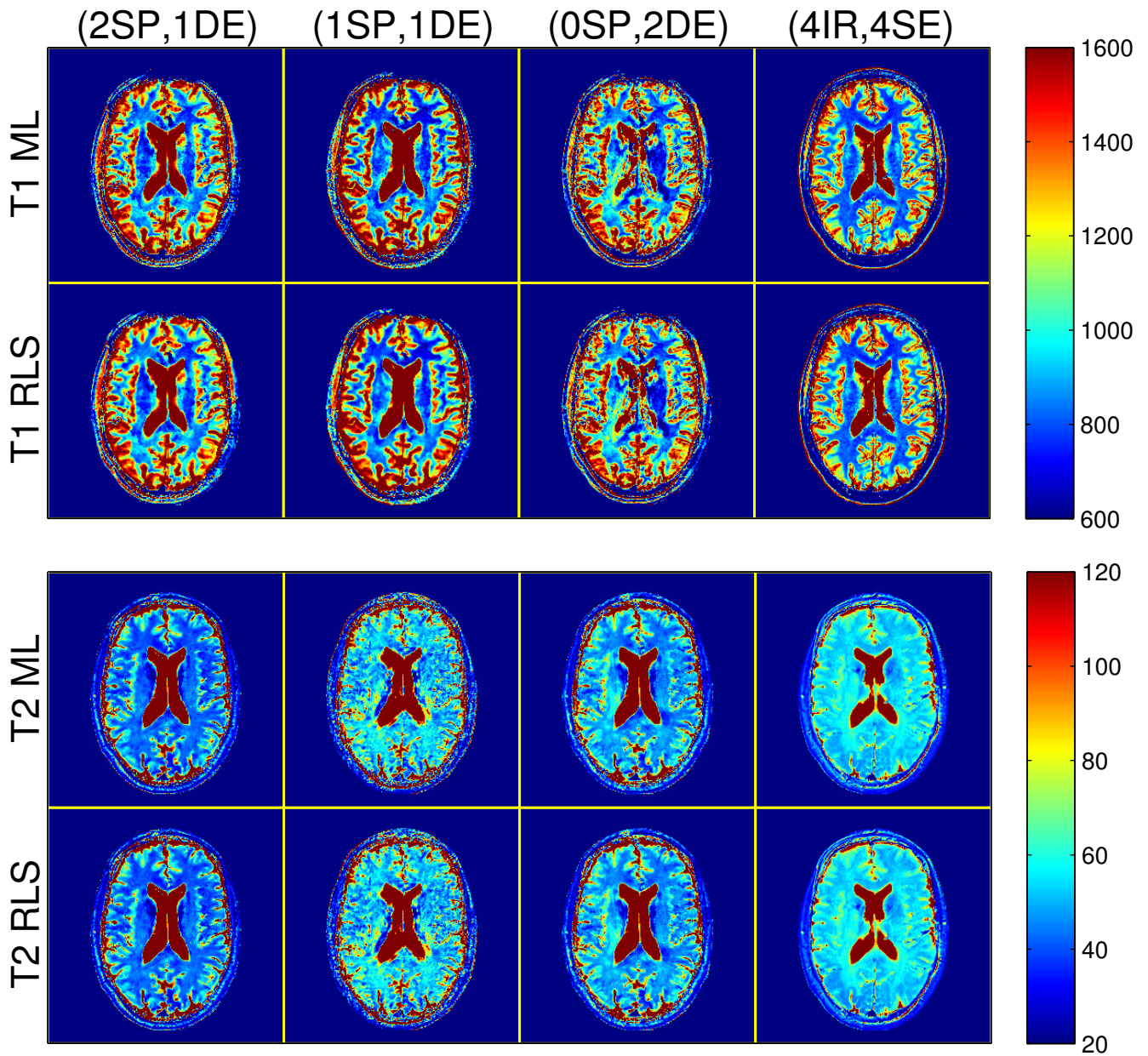


Figure S.9: Grayscale T_1 and T_2 ML and RLS estimates from the brain of a healthy volunteer. Columns correspond to profiles consisting of (2 SPGR, 1 DESS), (1 SPGR, 1 DESS), (0 SPGR, 2 DESS), and (4 IR, 4 SE) acquisitions. Rows distinguish T_1 and T_2 ML and RLS estimators. Fig. S.10 provides identical grayscale images. Colorbar ranges are in milliseconds.

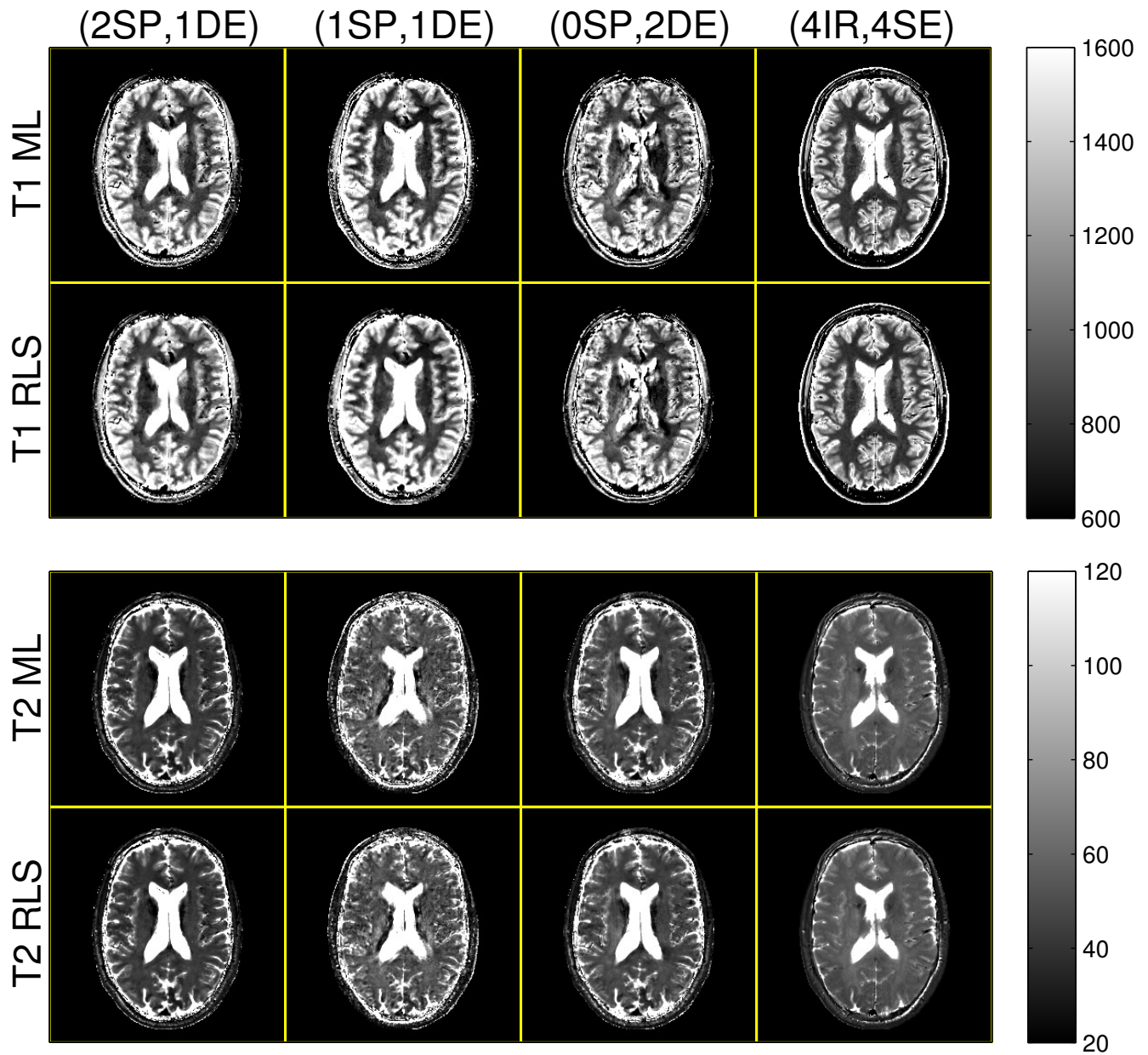


Figure S.10: Grayscale T_1 and T_2 ML and RLS estimates from the brain of a healthy volunteer. Columns correspond to profiles consisting of (2 SPGR, 1 DESS), (1 SPGR, 1 DESS), (0 SPGR, 2 DESS), and (4 IR, 4 SE) acquisitions. Rows distinguish T_1 and T_2 ML and RLS estimators. Fig. S.9 provides identical colorized images. Colorbar ranges are in milliseconds.

	ROI (color)	(2SP,1DE)	(1SP,1DE)	(0SP,2DE)	(4IR,4SE)
\hat{T}_1^{RLS}	anterior right WM (yellow)	840 ± 24	770 ± 20.	840 ± 43	780 ± 20.
	anterior left WM (magenta)	740 ± 51	670 ± 37	740 ± 54	760 ± 23
	posterior right WM (green)	890 ± 79	860 ± 61	960 ± 82	810 ± 24
	posterior left WM (blue)	870 ± 62	850 ± 50.	880 ± 78	820 ± 35
	anterior GM (cyan)	1200 ± 200	1200 ± 220	1300 ± 230	1300 ± 180
\hat{T}_2^{RLS}	anterior right WM (yellow)	40. ± 1.3	54 ± 3.4	46 ± 1.5	55 ± 1.9
	anterior left WM (magenta)	40. ± 1.7	50. ± 4.4	43 ± 1.7	53 ± 1.8
	posterior right WM (green)	43 ± 2.8	60. ± 6.7	51 ± 3.7	58 ± 2.3
	posterior left WM (blue)	43 ± 1.7	57 ± 4.7	49 ± 2.5	57 ± 1.8
	anterior GM (cyan)	50 ± 12	60 ± 15	60 ± 11	59 ± 6.4

Table S.3: Within-ROI sample means \pm within-ROI sample standard deviations of \mathbf{T}_1 and \mathbf{T}_2 RLS estimates from the brain of a healthy volunteer. Sample statistics are computed within ROIs indicated in Fig. 2. All values are reported in milliseconds.

	ROI (color)	$[10, 30]^T$	$[10, 60]^T$	$[10, 150]^T$
\hat{T}_2^{ML}	anterior right WM (yellow)	54 ± 3.0	56 ± 1.9	54 ± 2.4
	anterior left WM (magenta)	50. ± 2.2	54 ± 1.8	54 ± 2.4
	posterior right WM (green)	55 ± 2.6	58 ± 2.2	61 ± 2.6
	posterior left WM (blue)	50 ± 2.2	57 ± 2.0	61 ± 2.1
	anterior GM (cyan)	58 ± 6.5	61 ± 6.8	57 ± 7.3

Table S.4: Within-ROI sample means \pm within-ROI sample standard deviations of monoexponential \mathbf{T}_2 ML estimates, from pairs of *in vivo* SE datasets. Column headers indicate echo times \mathbf{T}_E (ms) of SE datasets. Sample statistics are computed within ROIs indicated in Fig. 2. Single-component \hat{T}_2^{ML} estimates in WM depend on SE echo times.

This section explores the effect of model mismatch due to multi-component relaxation on single-component \mathbf{T}_2 estimation bias, through numerical simulations and *in vivo* experiments.

We simulate multi-exponential data to arise from three non-exchanging pools of myelinated water $(T_1, T_2) \leftarrow (500, 20)\text{ms}$, intracellular and extracellular water $(T_1, T_2) \leftarrow (1000, 80)\text{ms}$, and free water $(T_1, T_2) \leftarrow (3500, 250)\text{ms}$ [23, 24]. We assign pool fractions of $(0.15, 0.80, 0.05)$ in WM and $(0, 0.95, 0.05)$ in GM to the 81st slice of the BrainWeb digital phantom [25, 26] to create ground truth \mathbf{M}_0 , \mathbf{T}_1 , and \mathbf{T}_2 compartment-wise maps. We simulate component-wise IR signals (acquisition parameters in Section IV.B.1) and add them to yield noiseless multi-component IR data. We likewise simulate and then add component-wise SE signals to construct three scan profiles consisting of pairs of multi-component SE datasets with variable $\mathbf{T}_E \in \{[10, 30]^T, [10, 60]^T, [10, 150]^T\}$. To avoid confounding sources of bias, we assume knowledge of a uniform transmit field and a uniform sensitivity profile of a single-channel receive coil. We estimate a single-component $\hat{\mathbf{T}}_1$ ML map from multi-component IR data, which we then use to estimate a single-component $\hat{\mathbf{T}}_2$ ML map from each multi-exponential SE scan profile.

The upper rows of Figs. S.11 and S.12 compare (in color and grayscale) $\hat{\mathbf{T}}_2$ maps from simulated multi-exponential SE data. The lower rows compare *in vivo* $\hat{\mathbf{T}}_2$ maps from corresponding subsets of the SE reference profile discussed in Section IV.C. As echo times are further separated, $\hat{\mathbf{T}}_2$ in WM approaches $\hat{\mathbf{T}}_2$ in GM, creating an apparent reduction in $\hat{\mathbf{T}}_2$ WM/GM contrast.

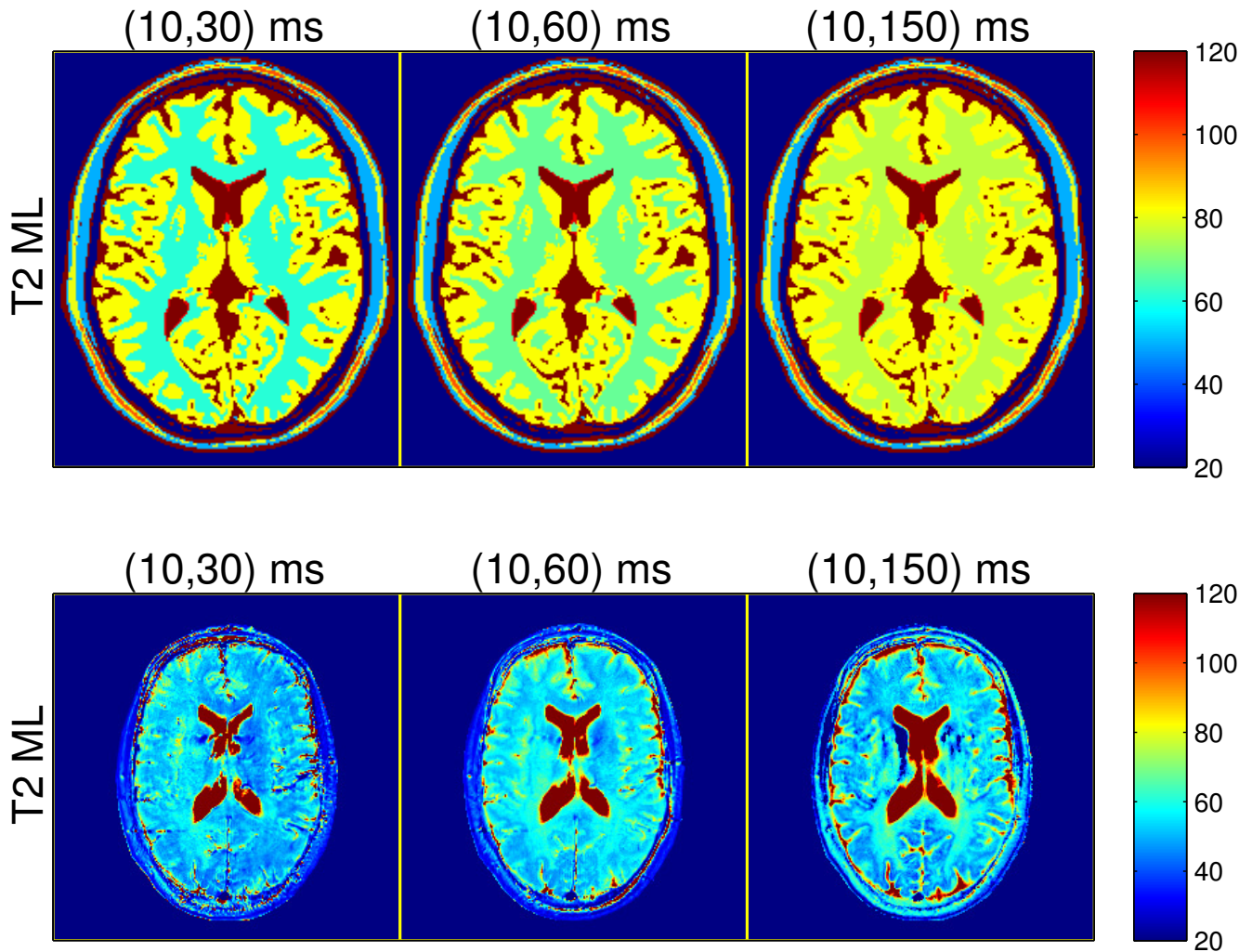


Figure S.11: Colorized monoexponential T_2 ML estimates from pairs of (top) multi-exponential simulated and (bottom) *in vivo* SE datasets. Columns denote SE dataset echo times. Fig. S.12b provides identical grayscale images. Colorbar ranges are in milliseconds.

Table S.4 summarizes \hat{T}_2^{ML} sample means and sample standard deviations (computed within WM/GM ROIs depicted in Fig. 2) from *in vivo* SE scan profiles. Single-component \hat{T}_2^{ML} estimates depend on SE echo times more significantly in WM than in GM. Comparing with Table IV, trends suggest that disagreement in \hat{T}_2^{ML} estimates across scan profiles may in part be attributable to the substantial differences of acquisition parameters (*e.g.* echo time) used in different pulse sequences.

References

- [1] G. Nataraj, J.-F. Nielsen, and J. A. Fessler, “Optimizing MR scan design for model-based T_1 , T_2 estimation from steady-state sequences,” *IEEE Trans. Med. Imag.*, 2016, to appear.
- [2] H. Z. Wang, S. J. Riederer, and J. N. Lee, “Optimizing the precision in T_1 relaxation estimation using limited flip angles,” *Mag. Res. Med.*, vol. 5, no. 5, pp. 399–416, Nov. 1987.
- [3] L. Fleysler, R. Fleysler, S. Liu, W. Zaaraoui, and O. Gonen, “Optimizing the precision-per-unit-time of quantitative MR metrics: Examples for T_1 , T_2 , and DTI,” *Mag. Res. Med.*, vol. 57, no. 2, pp. 380–7, Feb. 2007.

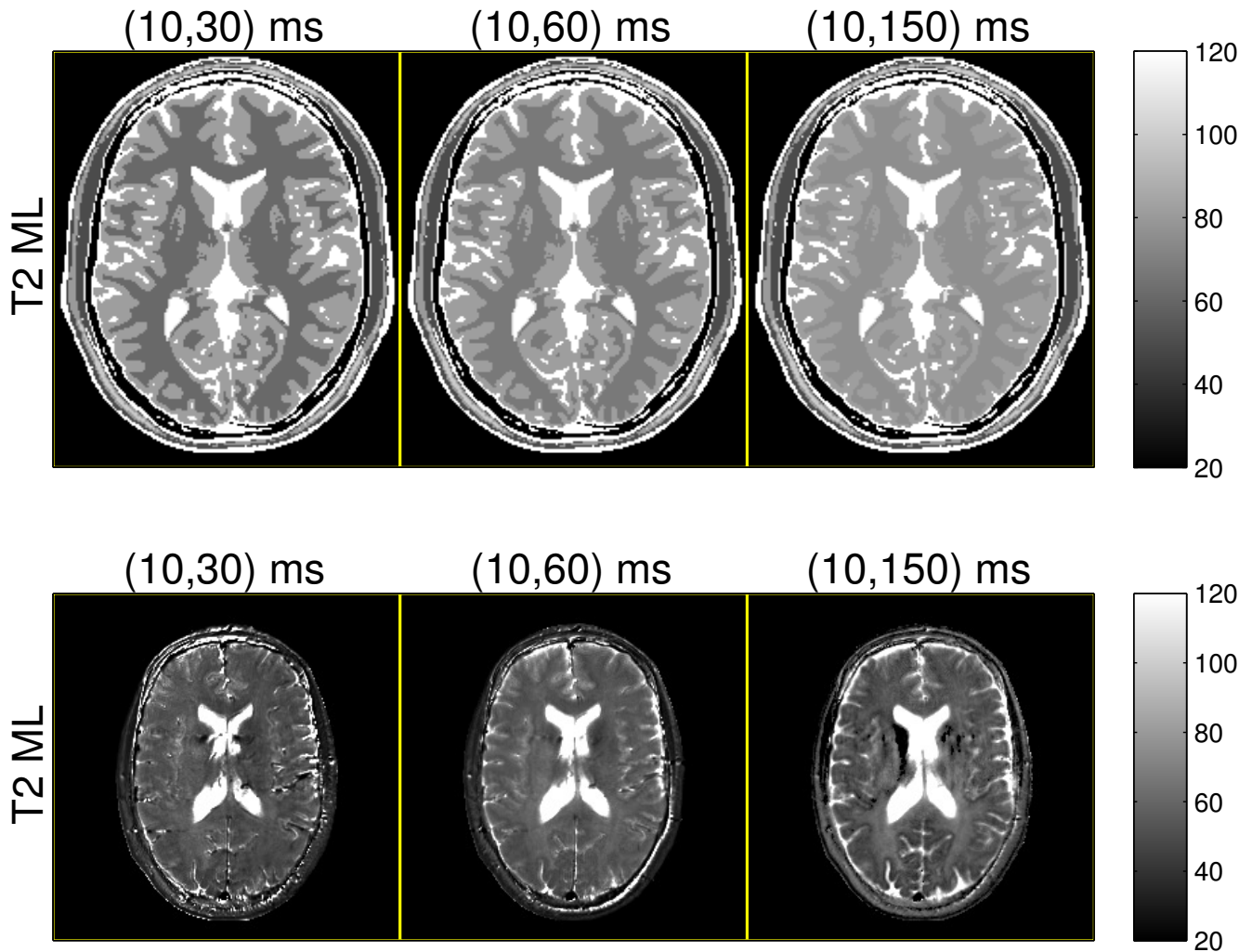


Figure S.12: Grayscale monoexponential T_2 ML estimates from pairs of (top) multi-exponential simulated and (bottom) *in vivo* SE datasets. Columns denote SE dataset echo times. Fig. S.11b provides identical colored images. Colorbar ranges are in milliseconds.

- [4] J. Imran, François. Langevin, and Hervé. Saint-Jalmes, “Two-point method for T1 estimation with optimized gradient-echo sequence,” *Mag. Res. Im.*, vol. 17, no. 9, pp. 1347–56, Nov. 1999.
- [5] S. C. L. Deoni, B. K. Rutt, and T. M. Peters, “Rapid combined T1 and T2 mapping using gradient recalled acquisition in the steady state,” *Mag. Res. Med.*, vol. 49, no. 3, pp. 515–26, Mar. 2003.
- [6] S. C. L. Deoni, T. M. Peters, and B. K. Rutt, “Determination of optimal angles for variable nutation proton magnetic spin-lattice, T_1 , and spin-spin, T_2 , relaxation times measurement,” *Mag. Res. Med.*, vol. 51, no. 1, pp. 194–9, Jan. 2004.
- [7] C. Kanzow, N. Yamashita, and M. Fukushima, “Levenberg-Marquardt methods with strong local convergence properties for solving nonlinear equations with convex constraints,” *J. Comp. Appl. Math.*, vol. 172, no. 2, pp. 375–97, Dec. 2004.
- [8] G. Golub and V. Pereyra, “Separable nonlinear least squares: the variable projection method and its applications,” *Inverse Prob.*, vol. 19, no. 2, pp. R1–26, Apr. 2003.
- [9] S. G. Mallat and Z. Zhang, “Matching pursuits with time-frequency dictionaries,” *IEEE Trans. Sig. Proc.*, vol. 41, no. 12, pp. 3397–415, Dec. 1993.
- [10] J. P. Haldar, J. Anderson, and S. W. Sun, “Maximum likelihood estimation of T1 relaxation parameters using VARPRO,” in *Proc. Intl. Soc. Mag. Res. Med.*, 2007, p. 41. [Online]. Available: <http://cds.ismrm.org/ismrm-2007/files/00041.pdf>
- [11] J. A. Fessler, “Mean and variance of implicitly defined biased estimators (such as penalized maximum likelihood): Applications to tomography,” *IEEE Trans. Im. Proc.*, vol. 5, no. 3, pp. 493–506, Mar. 1996.

- [12] H. Gudbjartsson and S. Patz, "The Rician distribution of noisy MRI data," *Mag. Res. Med.*, vol. 34, no. 6, pp. 910–4, Dec. 1995.
- [13] L. I. Sacolick, F. Wiesinger, I. Hancu, and M. W. Vogel, "B1 mapping by Bloch-Siegert shift," *Mag. Res. Med.*, vol. 63, no. 5, pp. 1315–22, May 2010.
- [14] E. K. Insko and L. Bolinger, "Mapping of the radiofrequency field," *J. Mag. Res. A*, vol. 103, no. 1, pp. 82–5, Jun. 1993.
- [15] L. Friedman and G. H. Glover, "Report on a multicenter fMRI quality assurance protocol," *J. Mag. Res. Im.*, vol. 23, no. 6, pp. 827–39, Jun. 2006.
- [16] L. Ying and J. Sheng, "Joint image reconstruction and sensitivity estimation in SENSE (JSENSE)," *Mag. Res. Med.*, vol. 57, no. 6, pp. 1196–1202, Jun. 2007.
- [17] H. Sun, W. A. Grissom, and J. A. Fessler, "Regularized estimation of Bloch-Siegert B1+ Maps in MRI," in *Proc. IEEE Intl. Conf. on Image Processing*, 2014, pp. 3646–50.
- [18] A. Funai, J. A. Fessler, W. Grissom, and D. C. Noll, "Regularized B1+ map estimation in MRI," in *Proc. IEEE Intl. Symp. Biomed. Imag.*, 2007, pp. 616–9.
- [19] D. Arthur and S. Vassilvitskii, "K-means++: The advantages of careful seeding," in *Proc. 18th Annual ACM-SIAM Symp. Disc. Alg. (SODA)*, 2007, pp. 1027–35. [Online]. Available: <http://dl.acm.org/citation.cfm?id=1283494>
- [20] J. K. Barral, E. Gudmundson, N. Stikov, M. Etezadi-Amoli, P. Stoica, and D. G. Nishimura, "A robust methodology for in vivo T1 mapping," *Mag. Res. Med.*, vol. 64, no. 4, pp. 1057–67, Oct. 2010.
- [21] L. R. Frank, E. C. Wong, and R. B. Buxton, "Slice profile effects in adiabatic inversion: Application to multislice perfusion imaging," *Mag. Res. Med.*, vol. 38, no. 4, pp. 558–64, Oct. 1997.
- [22] K. E. Keenan, K. F. Stupic, M. A. Boss, S. E. Russek, T. L. Chenevert, P. V. Prasad, W. E. Reddick, K. M. Cecil, J. Zheng, P. Hu, and E. F. Jackson, "Multi-site, multi-vendor comparison of T1 measurement using ISMRM/NIST system phantom," in *Proc. Intl. Soc. Mag. Res. Med.*, 2016, p. 3290.
- [23] A. Mackay, K. Whittall, J. Adler, D. Li, D. Paty, and D. Graeb, "In vivo visualization of myelin water in brain by magnetic resonance," *Mag. Res. Med.*, vol. 31, no. 6, pp. 673–7, Jun. 1994.
- [24] S. C. L. Deoni, L. Matthews, and S. H. Kolind, "One component? Two components? Three? The effect of including a nonexchanging "free" water component in multicomponent driven equilibrium single pulse observation of T1 and T2," *Mag. Res. Med.*, vol. 70, no. 1, pp. 147–54, Jul. 2013.
- [25] R. K.-S. Kwan, A. C. Evans, and G. B. Pike, "MRI simulation-based evaluation of image-processing and classification methods," *IEEE Trans. Med. Imag.*, vol. 18, no. 11, pp. 1085–97, Nov. 1999.
- [26] D. L. Collins, A. P. Zijdenbos, V. Kollokian, J. G. Sled, N. J. Kabani, C. J. Holmes, and A. C. Evans, "Design and construction of a realistic digital brain phantom," *IEEE Trans. Med. Imag.*, vol. 17, no. 3, pp. 463–8, Jun. 1998.